AGU PUBLICATIONS

Tectonics

RESEARCH ARTICLE
10.1002/2016TC004408

Key Points:
- Eclogitization of a Cambrian (~530 Ma) ophiolitic block occurred at ~490 Ma
- Hf isotopes from zircon suggest an intra-oceanic setting
- Addition of juvenile oceanic crust to continental margins is an important mechanism of continental growth

Supporting Information:
- Supporting Information S1

Correspondence to:
R. J. Manton,
rjm828@uowmail.edu.au

Citation:
Manton, R. J., S. Buckman, A. Nutman, V. Bennett, and E. Belousova (2017), U-Pb-Hf-REE-Ti zircon and REE garnet geochemistry of the Cambrian Attunga eclogite, New England Orogen, Australia: Implications for continental growth along eastern Gondwana, *Tectonics*, *36*, 1580–1613, doi:10.1002/2016TC004408.

Received 3 NOV 2016
Accepted 20 JUL 2017
Accepted article online 27 JUL 2017
Published online 26 AUG 2017

U-Pb-Hf-REE-Ti zircon and REE garnet geochemistry of the Cambrian Attunga eclogite, New England Orogen, Australia: Implications for continental growth along eastern Gondwana

Ryan J. Manton[1], Solomon Buckman[1], Allen P. Nutman[1], Vickie C. Bennett[2], and Elena A. Belousova[3]

[1]GeoQuEST Research Centre, School of Earth and Environmental Sciences, University of Wollongong, Wollongong, New South Wales, Australia, [2]Research School of Earth Sciences, Australian National University, Canberra, ACT, Australia, [3]GEMOC, Macquarie University, North Ryde, New South Wales, Australia

Abstract The timing and location of eclogite metamorphism is central to understanding subduction events responsible for the assembly of eastern Gondwana. The Attunga eclogite is one of only six eclogites in Australia and occurs as small blocks within a schistose serpentinite mélange known as the Weraerai terrane, along the Peel Fault of the southern New England Orogen. Our zircon data reveal the presence of high Th/U oscillatory zoned magmatic zircon with a weighted mean $^{206}Pb/^{238}U$ age of 534 ± 14 Ma and recrystallized metamorphic domains with an age of 490 ± 14 Ma. The latter have lower Th/U ratios, mostly no Eu anomalies and heavy rare earth element (HREE)-depleted patterns. Garnet rims demonstrate that the final stages of garnet growth occurred in a HREE-depleted environment, due to coeval formation with metamorphic zircon. Direct application of the Ti-in-zircon thermometer to metamorphic zircon yields temperatures of 770–610°C. Hf isotopic analyses of the zircons have an average $\varepsilon Hf_{(t)}$ of +13, indicating a juvenile crustal signature. We interpret the Attunga eclogite to be an indicator of Late Cambrian subduction beneath an oceanic suprasubduction zone prior to accretion against eastern Gondwanan in the latest Devonian. Phillips et al. (2015) suggest two metamorphic age populations within the Attunga eclogite, based on U-Pb zircon and $^{40}Ar/^{39}Ar$ phengite data. These are ~515 Ma and ~480 Ma. We confirm these data, but our zircon trace element chemistry data indicate that the Early Cambrian age (530 Ma) represents igneous protolith formation rather than eclogite metamorphism.

1. Introduction

Blueschists and associated eclogites are signature metamorphic rocks from low metamorphic thermal gradients associated with subduction [*Ernst*, 1970, 1972; *Goffé and Chopin*, 1986; *Maruyama et al*., 1996; *Ernst*, 2001]. In ancient terranes, they are important indicators of former convergent plate boundaries and associated sutures [*Ernst*, 1988; *Hacker et al*., 2003; *Ota and Kaneko*, 2010]. However, they become rarer in early Paleozoic and older orogens due to loss by erosion or subsequent retrograde overprinting metamorphism [e.g., *Brown*, 2009]. Thus, tectonic reconstructions that include several discrete subduction events involving obduction or arc collisions onto continental margins become increasingly difficult to recognize. Age determinations on minerals grown or recrystallized during high-pressure metamorphism can be achieved by applying U-Pb dating of metamorphic zircon growths or Sm-Nd determinations on coexisting garnet and omphacite [e.g., *Hermann et al*., 2001; *Gilotti et al*., 2004; *Nutman et al*., 2008]. Geochronology that distinguishes different ages of such metamorphic events within single orogens provides important constraints on accurate tectonic reconstructions [*Di Vinchenzo et al*., 1997; *Rubatto et al*., 1999; *Gilotti et al*., 2004; *Hacker et al*., 2006; *Cheng et al*., 2012; *Zhai et al*., 2013].

The Australian continent is host to only six known eclogite occurrences. Five of these occur within the Paleozoic Tasmanides [*Glen*, 2013] (Figure 1), with only one occurrence within shear zones of the Meso-Neoproterozoic Musgrave Block, Central Australia [*Camacho et al*., 1997]. The Tasmanides represent significant continental growth throughout the Paleozoic along the eastern Gondwana margin [*Cawood*, 2005], and rare eclogites and blueschists represent important "road signs" in the spatial and temporal evolution of eastern Gondwana. Two eclogite localities within the Tasmanian portion of the Lachlan Orogen are the Franklin and Forth Complexes with a U-Pb zircon metamorphic age of 514–504 Ma [*Black et al*., 1997;

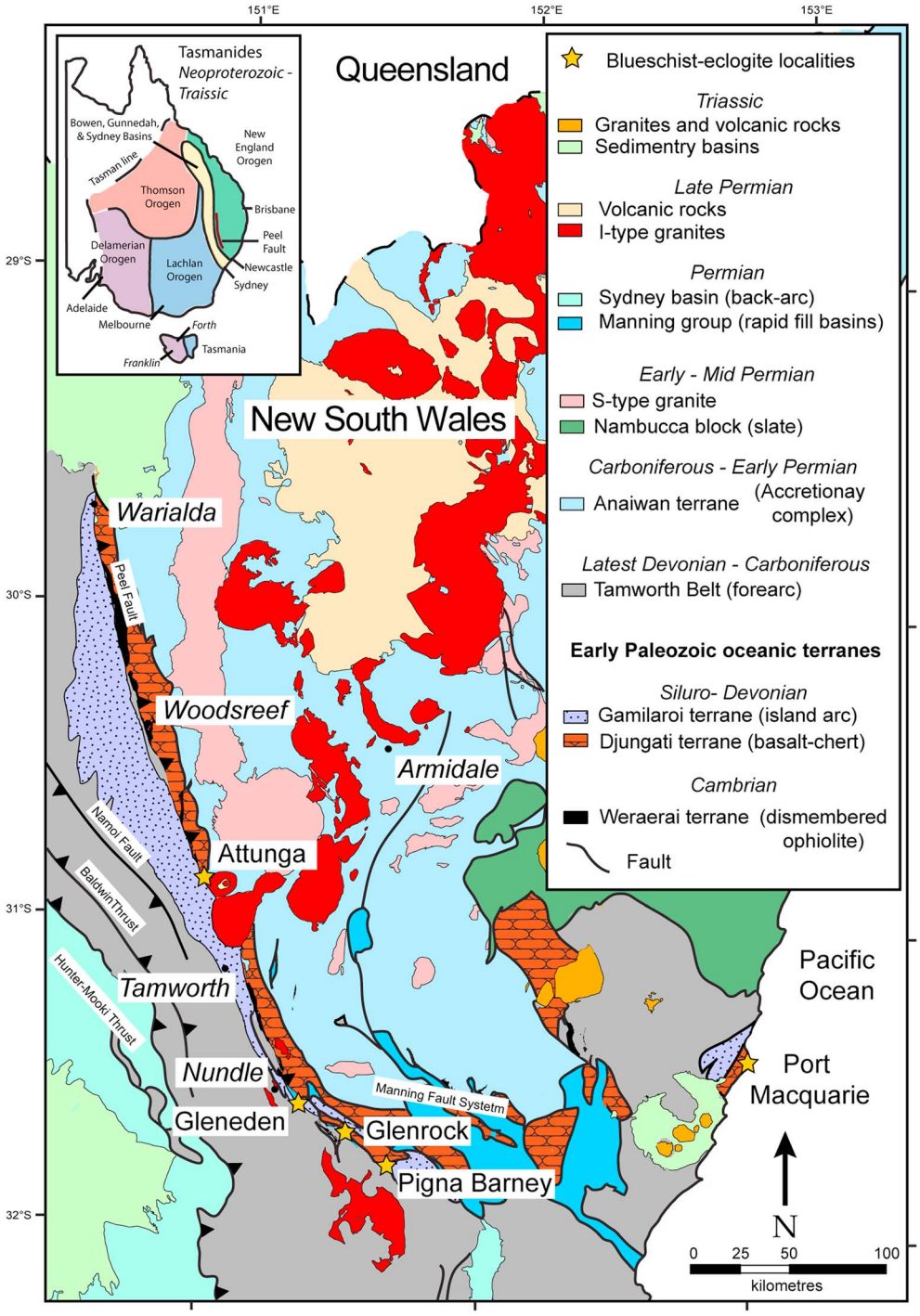

Figure 1. Regional geology of the Attunga area. Units grouped into terrane scheme of [*Flood and Aitchison*, 1988]. Tasmanides classification after *Glen* [2005]. Source of map: NSW Geological Survey Seamless Geology Project, UTM Zone 56.

Fergusson et al., 2013]. The other three occur in the southern New England Orogen, NSW (Figure 1). Two exotic blocks within a serpentinite mélange are intimately associated with the Weraerai terrane (Great Serpentine Belt) at Attunga [*Shaw and Flood*, 1974; *Watanabe et al.*, 1999; *Phillips et al.*, 2015] and Gleneden [*Allan and Leitch*, 1992], and the third is at Port Macquarie on the coast (Figure 1) [*Fukui et al.*, 1995; *Och et al.*, 2003, 2007; *Nutman et al.*, 2013]. Also, two lawsonite-bearing blueschists are located within the serpentinite mélange at Glenrock and Pigna Barney [*Fukui et al.*, 1995; *Offler*, 1999; *Fukui et al.*, 2012; *Phillips et al.*, 2015]. Their relevance to the Attunga eclogite will be discussed briefly.

This paper presents an integrated field, petrographic and zircon U-Th-Pb-Hf-REE-Ti and garnet geochemistry study of the Attunga eclogite. Cambrian ages are derived for both the protolith and the superimposed eclogite facies metamorphic event. Zircon initial εHf values indicate the juvenile crustal nature of these rocks and suggest that they formed in the Panthalassa (Paleo-Pacific) intra-oceanic realm before being accreted onto the Gondwanan margin. Recently, *Phillips et al*. [2015] obtained two Cambrian zircon age populations from the Attunga eclogite (~515 and ~490 Ma) and interpreted both as separate eclogitic metamorphic events associated with a single, long-lived, westerly dipping subduction event that started with the Delamerian Orogeny in South Australia and was responsible for the formation of the entire Paleozoic Tasmanides of eastern Australia. Our results show that the older Cambrian (~515 Ma) zircon population are, in fact, relict igneous zircons derived from the ophiolitic protolith of the Weraerai terrane which has a well-established and similar age of 520–530 Ma [*Aitchison and Ireland*, 1995]. Whilst our zircon ages are in general agreement with those of *Phillips et al*. [2015], we provide additional zircon Hf isotope data that demonstrate the juvenile, intra-oceanic origins of the eclogitized ophiolitic rocks at Attunga. These conflicting interpretations have important ramifications for crustal growth mechanisms and the incorporation of Cambrian crustal terranes within younger Devonian-Carboniferous crustal rocks of the New England Orogen along the eastern margin of Gondwana.

2. Geological Context

The eastern portion of Australia forms a segment of a 3000 km long orogenic belt on the margin of Gondwana, known alternatively as the Tasman Orogenic Zone [*Zucchetto et al*., 1999] or the Tasmanides [*Scheibner and Basden*, 1996; *Cawood and Buchan*, 2007; *Kemp et al*., 2009; *Glen*, 2013]. From west to east the Tasmanides (Figure 1) are subdivided into three distinct orogens: (i) the Delamerian/Ross Orogen (Neoproterozoic-Early Ordovician) [*Haines et al*., 2009], (ii) the Lachlan Orogen (Cambrian-Devonian) [*Fergusson and Coney*, 1992; *Gray and Foster*, 2004], and (iii) the New England Orogen (early Paleozoic-Mesozoic) [*Leitch*, 1975]. The Thomson Orogen in QLD is largely covered by Mesozoic sediments, and due to limited outcrop, its structural elements are poorly understood [*Glen*, 2005]. Because of this, it will not be included here in the outline of the Tasmanides. An interpretation of the mentioned orogens is that they developed via periodic steepening and flattening of a continuously westerly dipping subduction zone resulting in the opening and closing of back-arc basins behind a series of arcs that developed close to the eastern margin of Gondwana (summarized by *Collins* [2002], *Cawood* [2005], and *Glen* [2005]). This long-held and widely accepted model has been challenged by *Crawford et al*. [2003], *Aitchison and Buckman* [2012], and *Buckman et al*. [2014a] who proposed that various intra-oceanic ophiolitic and island arc complexes exotic to Gondwana collided and accreted with the eastern margin of Gondwana via alternating periods of east and west directed subduction (Figure 2).

2.1. Delamerian and Lachlan Orogens

The Australian Delamerian Orogen (Antarctica equivalent being the Ross Orogen) involved subduction along the eastern margin Gondwana from 514 to 499 Ma (Figure 2a) [*Coney*, 1990; *Foster and Gray*, 2000; *Glen*, 2005; *Robertson et al*., 2015]. It is characterized by a deformed sequence of Neoproterozoic to Cambrian Adelaide rift to passive margin sedimentary rocks [*Glen et al*., 2009; *Cayley*, 2011]. Termination of the Delamerian Orogeny is marked by rapid uplift and the emplacement of A-type granites at ~490 Ma [*Foden et al*., 2006]. It has been suggested that the Delamerian Orogeny may be linked with the formation of Cambrian ophiolites in the Lachlan and New England Orogen [*Cawood*, 2005; *Phillips and Offler*, 2011] as well as the formation of the Attunga eclogite [*Phillips et al*., 2015]. This hypothesis is examined in section 7.

Controversy surrounds the formation of the Lachlan Orogen (Figure 2c). Models range from a pure accretionary orogen with a single, long-lived, easterly retreating westerly dipping subduction zone [*Collins*, 2002; *Glen*, 2005; *Cawood et al*., 2009; *Glen and Meffre*, 2009; *Kemp et al*., 2009] to multiple subduction zones, of varying polarity [*Collins and Vernon*, 1992; *Fergusson*, 2003; *Spaggiari et al*., 2004; *Fergusson et al*., 2013]. The Macquarie Arc, a dismembered Ordovician island arc [*Glen et al*., 1998, 2007, 2011], is distributed across the central portion of the orogen. *Aitchison and Buckman* [2012] argue that this arc was accreted as an exotic terrane in the Early Silurian (~440 Ma) resulting in the Benambran Orogeny [*Glen et al*., 2007] and widespread deformation of the structurally underlying, passive margin sedimentary sequence (Adaminaby Group) on the Gondwana margin during overthrusting of the exotic Macquarie Arc. This arc-continental collision was followed by a

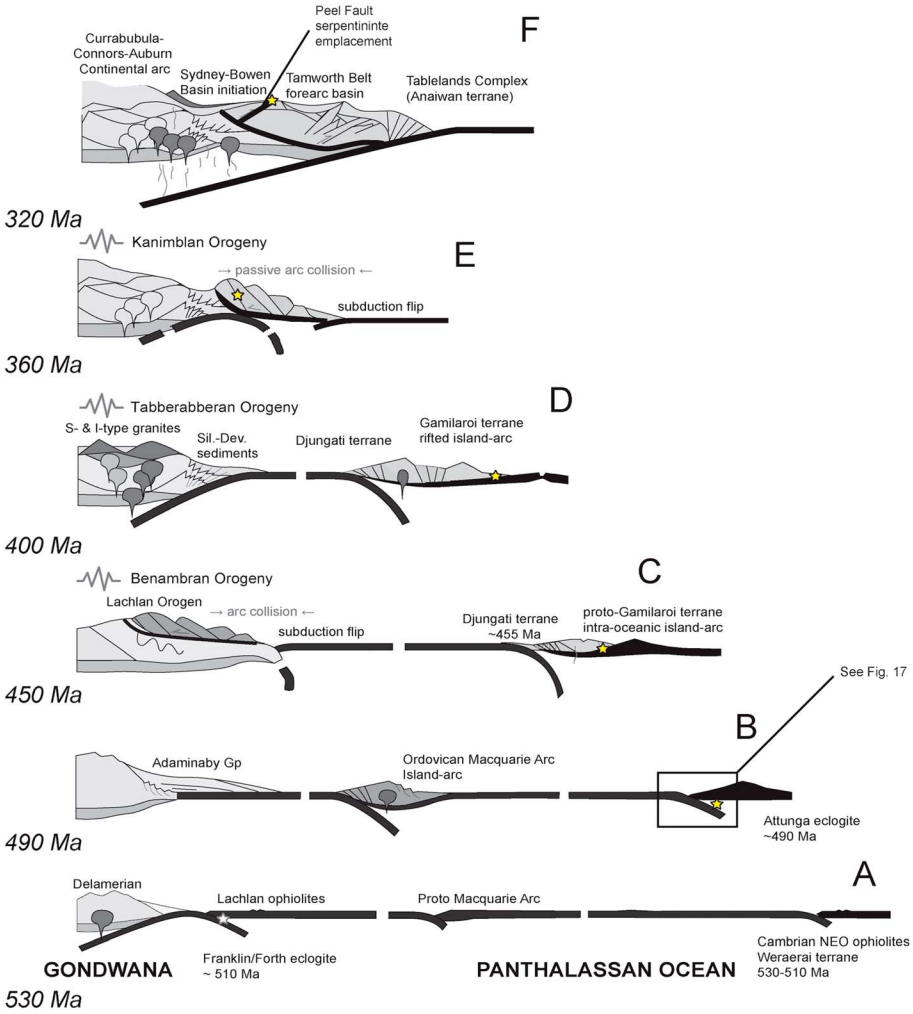

Figure 2. A schematic tectonic setting for the Tasmanides and the proposed formation setting for the Attunga eclogite. Adapted from *Buckman et al*. [2014a]. Our suggested location for the Attunga eclogite during the development for the east coast of Gondwana. (a) Formation of the Weraerai terrane ophiolite in a fore-arc setting during the Early Cambrian. The associated island arc has not been located. (b) Formation of the Attunga eclogite occurred at ~490 Ma, from the removal and subsequent eclogitization of the overlying suprasubduction basaltic units. (c) Chert accretionary complexes of the Djungati terrane formed during the Late Ordovician. It is possible the later (Siluro-Devonian) oceanic island arc Gamilaroi terrane is built on early Paleozoic units. It is likely that the preservation of the Attunga eclogite and the Weraerai terrane occurred during this period. (d) Rifting of the Gamilaroi terrane occurs with continual accretion of chert in the Djungati terrane. (e) Accretion of the Gamilaroi terrane onto the Gondwanan margin occurred in the latest Devonian. During this period, the emplacement of granitic intrusive bodies into Lachlan Orogen ceased. (f) The serpentinite mélange, containing the Weraerai terrane and the Attunga eclogite, was emplaced along the Peel Fault in the Early Permian.

subduction flip and onset of a typical Andean-type continental convergent margin and onset of the Tabberabberan Orogeny throughout the Silurian to Devonian [*Cas*, 1983; *Powell*, 1984]. Orogenic activity and magmatism within the Lachlan Orogen abruptly switched off in the latest Devonian after the Kanimblan Orogeny, an event that is proposed to mark the collision of the island arc Gamilaroi terrane island arc and the beginning of the New England Orogen [*Aitchison and Flood*, 1994; *Buckman et al*., 2014b; *Flood and Aitchison*, 1988].

2.2. New England Orogen

The southern New England Orogen in NSW (as opposed to the northern New England Orogen in QLD) is dominated by Carboniferous continental convergent margin sequences, which formed above a west dipping subduction zone. The orogen is a tectonic collage [*Buckman et al*., 2014b] of Carboniferous continental

margin arc and material deposited on older Ordovician-Devonian island arc terranes (Figure 1). Initiation of the New England Orogen started in the late Silurian, with the attenuation of an intra-oceanic island arc, the Gamilaroi terrane (Figures 2c and 2d) [*Flood and Aitchison*, 1988], consisting of volcaniclastic units, felsic intrusive rocks, and basalts [*Stratford and Aitchison*, 1997]. This terrane is distributed along the Peel Fault for ~400 km, along with a red chert-dominated accretionary complex (the Djungati terrane). The collision and accretion of the Gamilaroi terrane may be responsible for the Kanimblan Orogeny in the Lachlan Orogen to the west (Figure 2e) [*Aitchison and Flood*, 1994]. The Early Cambrian low-Ti ophiolitic Weraerai terrane [*Aitchison and Ireland*, 1995] which was previously known as the Great Serpentinite Belt [*Benson*, 1913] is juxtaposed against the Gamilaroi terrane along the Peel Fault. The Weraerai terrane is a disrupted serpentinite matrix mélange and contains Cambrian ophiolitic fragments that represent the oldest rocks (Figure 1) and possibly the ocean basement to the Gamilaroi terrane [*Buckman et al*., 2014a].

Following the collision and accretion of the Gamilaroi terrane, the New England Orogen transformed into a classic continental Andean-type margin consisting of a Carboniferous volcanic arc (Currabubula-Connors-Aubaun arc), fore-arc sequences (Tamworth Belt), and an accretionary complex known as the Anaiwan terrane [*Flood and Aitchison*, 1988] or Tablelands Complex [*Caprarelli and Leitch*, 1998; *Roberts and Engel*, 1987]. The core of the Carboniferous volcanic arc is now largely hidden by the Permian Sydney-Bowen Basins [*McPhie*, 1987] (Figure 2f); however, the Tamworth Belt fore-arc sequences are observed uncomfortably overlying the Gamilaroi terrane [*Aitchison and Flood*, 1994].

Peraluminous S-type granitic suites were emplaced in to the accretionary Anaiwan terrane during the Early Permian [*Cawood et al*., 2011]. An increase of the geothermal gradient, leading to melting in the accretionary wedge, may have been caused by a more oblique convergent margin direction during this period [*Shaw and Flood*, 1981; *Aitchison and Flood*, 1992]. Oblique convergence may also have resulted in widespread strike-slip faulting and the development of small strike-slip basins (Manning Group or Barnard Basin) along the entire Peel Fault [*Aitchison et al*., 1997] and final emplacement of the serpentinite mélange to upper crustal levels. After a brief mid-Permian magmatic hiatus, largely orthogonal continental margin subduction recommenced during the Late Permian to Triassic, east of the current coastline [*Cawood*, 1984; *Bryant et al*., 1997]. This resulted in extensive emplacement of 255–225 Ma I-type granite and volcanic suites into the Carboniferous-Permian accretionary complex [*Shaw and Flood*, 1981].

2.3. Peel Fault

Deformation histories in chaotic mélange zones are difficult to interpret due to the heterogeneous nature of blocks in serpentinite mélange. S-C mylonites can be notoriously inconsistent in mélange zones, particularly around these rotated blocks, and are best considered as indicating the last sense of motion within the shear zone.

Corbett [1976] and then *Cawood* [1982] suggested that tightly folded oceanic derived units adjacent to the Peel Fault originally exhibited a strike parallel to the fault system. The formation of drag structures, as well as bending and displacement toward the east where the Peel Fault transitions into the Manning Fault System near Barry (Figure 1), was a result of several oblique sinistral strike-slip faults offset from the main fault. *Williams* [1979], *Offler and Williams* [1987], and *Offler et al*. [1989] undertook detailed studies of the serpentinite at Glenrock Station (Figure 1) and recorded evidence of sinistral strike-slip faulting. Alternatively, the en echelon geometry of similar strike-slip basins at Barry and Glenrock and structural kinematic indicators, including tension gashes, suggest a dominantly dextral strike-slip regime during the Early Permian [*Scheibner and Glen*, 1972; *Aitchison et al*., 1997].

Devonian to Carboniferous rocks west of the Baldwin Thrust (Figure 1) in the western domain of the Tamworth Belt are only moderately deformed and characterized by gentle, upright northwest trending folds that have been refolded by later northeast trending folds [*Vickery et al*., 2010]. Deformation is increasingly intense in the Devonian Gamilaroi terrane closer to the Peel Fault. The eastern domain between the Namoi and Peel faults is characterized by open NNW trending folds overprinted by tight north trending folds developed during movement along the Peel Fault.

To the east of the Peel Fault, the Weraerai terrane is in fault contact with a thin sliver of isoclinally folded red ribbon-bedded cherts of the Siluro-Devonian Djungati terrane [*Vickery et al*., 2010]. Here the Peel Fault dips steeply to the east [*Korsch et al*., 1997]. This small sliver of Djungati terrane is in fault contact with the

latest Devonian to Carboniferous basalt-chert-turbidite units of the Anaiwan terrane, which represents the continental accretionary complex of the New England Orogen throughout the Carboniferous.

2.4. Disrupted Ophiolitic Weraerai Terrane

The Weraerai terrane in the southern New England Orogen extends some 300 km from Warialda in the north to Nundle in the south (Figure 1). It consists of a highly schistose serpentinite matrix with a steeply dipping foliation. Locally, at Bingara it is referred to as the Woodsreef mélange [*Vickery et al*., 2010] which consists of schistose serpentinite matrix anastomosing around lenticular phacoids of variable size and composition, including peridotite, dunite, pyroxenite, gabbro, dolertite, plagiogranite, basalt, and some sedimentary rocks and rare eclogite/blueschist metamorphic equivalents [*Offler*, 1999], which together resemble a dismembered ophiolite. It was originally mapped and described by *Benson* [1913]. *Wilkinson* [1969] and *Leitch* [1980] interpreted these rocks as "alpine-type" ultramafic rocks injected into higher crustal levels as a series of cold intrusions during the Early Permian. Detailed petrological and geochemical studies [*Cross*, 1983; *Cross et al*., 1987; *Blake and Murchey*, 1988; *Sano et al*., 2004] established that these rocks are dismembered fragments of an ophiolite sequence. The highly refractory Ti-poor nature of these intrusive rocks led *Aitchison and Ireland* [1995] and *Yang and Seccombe* [1997] to suggest that they formed in a fore-arc, supra-subduction zone setting. On this basis, *Flood and Aitchison* [1988] proposed that these rocks represent a separate lithotectonic entity, the Weraerai terrane. U-Pb dating of zircons from plagiogranite of the Weraerai terrane gave an age of 530 ± 6 Ma [*Aitchison et al*., 1992], identifying this dismembered ophiolite as the oldest unit in the southern New England Orogen. This age prompted a reevaluation [*Aitchison and Ireland*, 1995] of the tectonic models that invoke continuous, westerly dipping subduction, accreting progressively younger crust onto the eastern margin of Gondwana throughout the Paleozoic.

2.5. Attunga Eclogite Field Occurrence

The Attunga eclogite crops out 32 km north of Tamworth as small blocks within a serpentinite mélange (Woodsreef Mélange), which is collectively assigned to the Weraerai terrane [*Vickery et al*., 2010] (Figure 3, top). The eclogite outcrop at Attunga is limited to a road cutting on the Wisemans Arm Road (30°50′40″S, 150°54′45″E WGS84). A few large blocks of eclogite are strewn across the adjacent field within 30 m of the outcrop, suggesting that some eclogite remains as resistant, residual blocks on the erosion surface as the softer serpentinite host is more easily eroded away (for field outcrop image, see supporting information and Figure S1). A variable degree of retrograde amphibolitization of the eclogite is observed, but generally, the eclogite blocks are broadly uniform with no igneous crosscutting relationships [cf. *Watanabe et al*., 1999] (see section 7).

To the west, the Weraerai terrane is in fault contact with a small sliver of shallow marine diamictites of the Early Permian Kensington Formation correlated regionally with the Manning Group (Barnard Basin) [*Vickery et al*., 2010]. These localized depocenters developed as oblique-slip basins (negative flower structures) during the Early Permian [*Aitchison et al*., 1997]. These strata are moderately deformed, well cleaved, and generally in fault contact with surrounding units, and thus, the Early Permian depositional age constrains the maximum age of movement along the Peel Fault. Farther south the Inlet Monzonite intrudes and stitches the Peel Fault. Its age of ~248 Ma [*Shaw and Flood*, 1992] constrains the minimum age of movement for at least this portion of the Peel Fault.

North-south strands of serpentinite mélange extend from the Peel Fault into the Siluro-Devonian Djungati terrane and Carboniferous Anaiwan terrane. Near the locality of Attunga and farther north to Bingara these N-S strands contain Ordovician-Silurian basalt-turbidite-limestone units of the Glen Bell Formation (Dunmore terrane) [*Vickery et al*., 2010]. The relationship between these Ordovician-Silurian units the rocks contained within the Weraerai terrane is still largely untested.

3. Analytical Methods

3.1. Whole-Rock X-Ray Florescence and Inductively Coupled Plasma-Mass Spectrometry Analysis

Five samples, ATE01, ATE02, ATE04, ATE05, and ATE06, were subjected to petrographic and geochemical analysis. Samples were crushed using a Cr-Ni TEMA ring grinder. Fused buttons were made for X-ray fluorescence (XRF) major element analysis. Given the mafic compositions of the samples, 12% tetraborate plus 22% metaborate flux was used. The samples were oxidized by adding 5 mL of lithium nitrate solution and left at 60°C

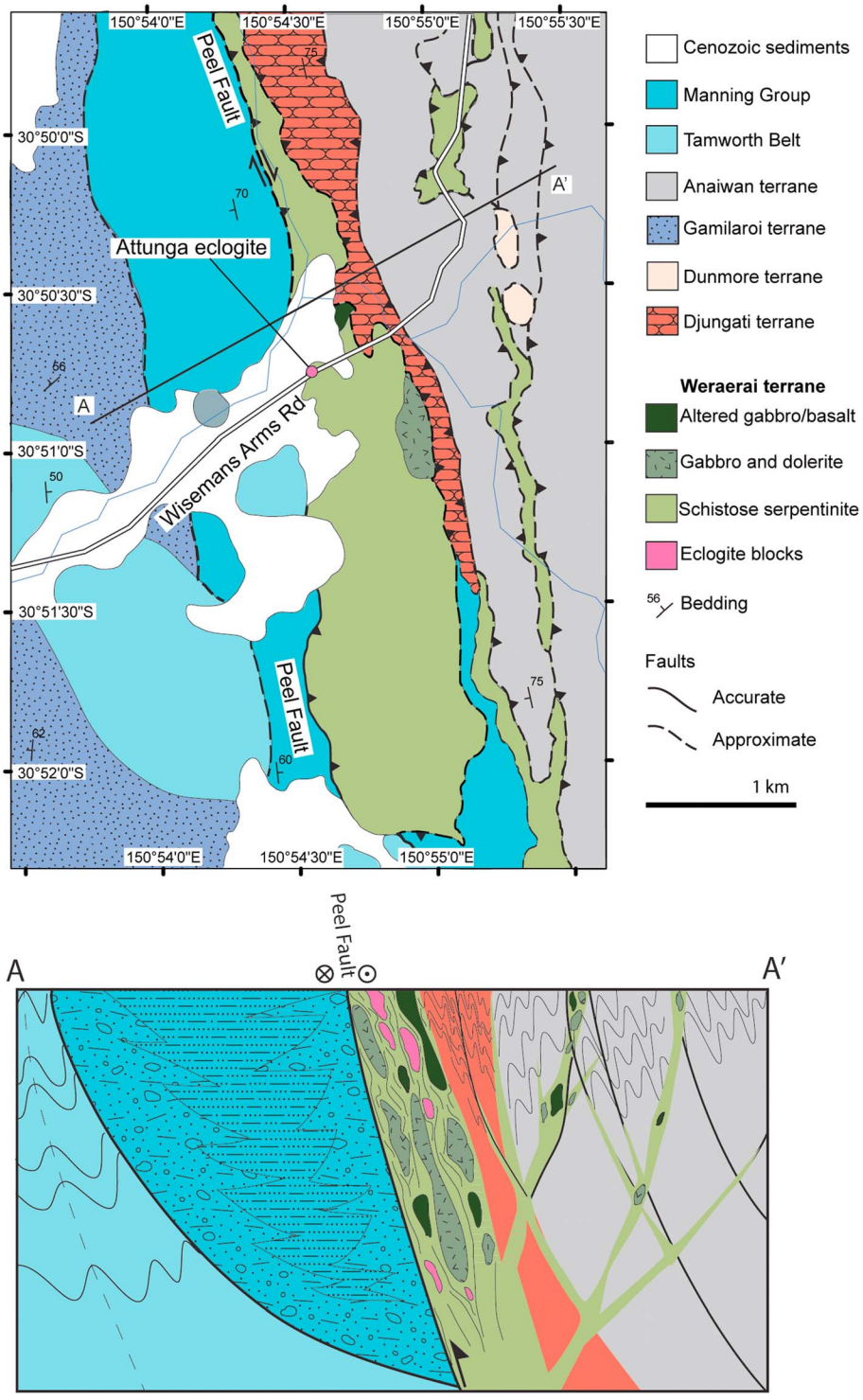

Figure 3. (top) Geology of the Attunga region. The eclogite block is located at 30°50′40″S, 150°54′45″E WGS84 on the side of the road at a bend in the Wisemans Arm Road. Source of map data is the NSW geological survey seamless geology project, UTM Zone 56. (bottom) Cross section across Peel Fault, based on data from *Blake and Murchey* [1988], *Jayko et al.* [1993], and *Aitchison et al.* [1997].

overnight, before being fused in a furnace. Pressed pellets for XRF trace element analysis were created by mixing ~5 g of sample with a polyvinyl acetate binder and pressed into an aluminum cup using a hydraulic hand press. Trace element pressed pellets were then oven dried at 60°C for 12 h. Whole-rock geochemical analysis was conducted using a SPECTRO XEPOS X-ray fluorescence spectrometer at the University of Wollongong. W-2 dolerite standard (n = 4) was used during the period that the data for this paper were acquired, which show a standard deviation of <3% for all the major elements and agree with accepted values.

Rare earth elements (REEs) were analyzed by ALS Minerals Division Brisbane via inductively coupled plasma-mass spectrometry (ICP-MS) (geochemical procedure ME-MS81). A prepared sample is added to lithium metaborate/lithium tetraborate flux, mixed well and fused in a furnace. The resulting melt is then cooled and dissolved in an acid mixture containing nitric, hydrochloric, and hydrofluoric acids. This solution is then analyzed by ICP-MS. Standards, OREAS 120 and STSD-1, were duplicated for the run as well as five sample duplicates and three blanks, with a 10% tolerance of error.

3.2. Mineral Microprobe Analysis

Mineral analyses were undertaken at Macquarie University on a Cameca SX50 electron microprobe with a voltage of 15 kV, sample current of 20 nA, and a beam spot size of 5 μm. Back-scatter electron images of selected sites were obtained on a JEOL JSM-490 LV at Wollongong Innovation Campus. Operating parameters were of 15 kV and a current of 5 nA.

3.3. Zircon Separation and Cathodoluminescence Imaging

The ATE01 zircon concentrate was prepared by standard heavy liquid and isodynamic Frantz magnetic separation techniques at the mineral separation laboratory of the Research School of Earth Sciences, the Australian National University (ANU). The concentrate was handpicked under a binocular microscope, and the selected grains were cast in epoxy resin discs together with the zircon Temora 2 reference material [*Black et al*., 2003]. The cured epoxy disc was ground to reveal midsections through the grains and then polished. The grains were documented with reflected and transmitted light photomicrographs and by cathodoluminescence (CL) imaging. Reconnaissance CL imaging was undertaken at the Australian National University, to guide the choice of sensitive high-resolution ion microprobe (SHRIMP) U-Pb analytical sites.

3.4. U-Pb Ion Microprobe Geochronology of Zircon

U-Pb geochronology was performed on the ANU SHRIMP II instrument. Analytical protocols followed *Williams* [1998], and reduction of the raw data used the ANU software "PRAWN" and "Lead." All errors also take into account nonlinear fluctuations in ion counting rates beyond that expected from counting statistics [*Stern*, 1998]. $^{206}Pb/^{238}U$ ratios of the unknowns were calibrated using measurements of the Temora 2 reference material (U-Pb ages concordant at 417 Ma) [*Black et al*., 2003] interspersed with analyses of the unknowns. In order to check for systematic bias in U-Pb calibration, several groups of Temora 2 were distributed across the mount. These were visited randomly during analysis and displayed no systematic differences. Therefore, the U-Pb ages on the Attunga zircon can be considered accurate. U and Th abundance was calibrated using measurement of the reference zircon SL13 (U = 238 ppm) located in an adjacent setup mount. Spot size on the zircons was 20 μm. The reduced and calibrated data were assessed and plotted using the ISOPLOT program of *Ludwig* [2003]. Weighted mean $^{206}Pb/^{238}U$ ages are reported at the 95% confidence level and are rounded to the nearest million years.

3.5. Zircon REE and Trace Element LA-ICP-MS

Rare earth element (REE) analyses of zircons were undertaken using LA-ICP-MS at GEMOC, Macquarie University Sydney, using a New Wave UP213 Nd:YAG 213 nm laser ablation system coupled to an Agilent 7700 quadrupole ICP-MS. *Jackson et al*. [2004] describe the setup, analysis, and analytical procedures for LA-ICP-MS. The data were calibrated against NIST 612 glass. Laser ablation spots were located atop SHRIMP pits, with later Lu-Hf LA-ICP-MS located beside them.

3.6. Garnet REE LA-ICP-MS

Garnet trace element analysis was carried out at GEMOC Macquarie University Sydney. A Photon Analyte G2 Excimer 193 nm laser coupled with Agilent 7700 ICP-MS was used for the analysis. Laser parameters were

5.69 J/m^2 at 5 Hz and a beam size of 50 μm. Average detection limits were 0.03 ppm. In run standards were NIST-610, U.S. Geological Survey basaltic glass standard BCR-2G, and Mongolian garnet MU5388 [*Norman et al*., 1996]. Offline data reduction was undertaken in GLITTER software with normalization of garnet analysis based on SiO_2 contents from microprobe data.

3.7. Zircon Lu-Hf Isotopic Measurements by LA-MC-ICP-MS

Zircon hafnium isotopic compositions were determined at the Research School of Earth Sciences, ANU, using a ThermoFinnigan Neptune multicollector ICP-MS coupled to a ArF λ = 193 nm eximer laser ablation system following methods described by *Hiess et al*. [2009]. The laser was focused to a 41 μm diameter spot and pulsed at 7 Hz with an energy density at the sample surface of ~5 J/cm^2, and jet sample cones were used in place of standard cones to enhance sensitivity. ^{171}Yb, ^{173}Yb, ^{174}Hf, ^{175}Lu, ^{176}Hf, ^{177}Hf, ^{178}Hf, ^{179}Hf, and ^{181}Ta isotopes were simultaneously measured in static-collection mode on nine Faraday cups with $10^{11}\Omega$ resistors. A large zircon crystal from the Monastery kimberlite was used to tune the mass spectrometer to optimum sensitivity. Analysis of a gas blank and a suite of secondary reference zircons (Mud Tank, FC1, and QGNG) were performed systematically after every 10–12 sample spot analyses.

Data were acquired in 1 s integrations over 100 s or until the grain burned through. Where possible the larger diameter laser spot was placed over the SHRIMP analysis spot. Offline segmental processing of the laser ablation data allowed detection of any downhole variation in Lu/Hf and ^{176}Hf/^{177}Hf related to drilling through different growth zones. During data reduction on a custom Excel™ spreadsheet, time slices were cropped to periods maintaining steady ^{176}Hf/^{177}Hf signals. Lu/Hf and ^{176}Hf/^{177}Hf ratios were uniform throughout data acquisition. Data reduction incorporated a within-run dynamic amplifier correction. Total Hf signal intensity typically fell from >14 to 6 V during a single analysis.

The measured ^{178}Hf/^{177}Hf, ^{176}Lu/^{177}Hf and ^{176}Hf/^{177}Hf ratios for the reference zircons are given in the supporting information Table S1. Mass bias was corrected using an exponential law [*Woodhead et al*., 2004] and a composition for ^{179}Hf/^{177}Hf of 0.732500 [*Patchett et al*., 1981]. Yb and Lu mass bias factors were assumed to be identical and normalized using an exponential correction to a ^{173}Yb/^{171}Yb ratio of 1.129197 [*Vervoort et al*., 2004]. The intensity of the ^{176}Hf peak was determined accurately by removing isobaric interferences from ^{176}Lu and ^{176}Yb. Interference-free ^{175}Lu and ^{173}Yb were measured and the interference peaks subtracted according to reported ^{176}Lu/^{175}Lu and ^{176}Yb/^{173}Yb isotopic abundances of *Vervoort et al*. [2004]. As a quality check of these procedures, ^{178}Hf/^{177}Hf and ^{174}Hf/^{177}Hf ratios for all zircon reference materials and samples are reported (Table S1). Average measured ^{176}Lu/^{177}Hf ratios within the reference zircons (Table S1) are in good agreement with the solution values reported by *Woodhead and Hergt* [2005].

The mean ^{176}Hf/^{177}Hf ratios for each of the reference zircons deviate from published solution values of *Woodhead and Hergt* [2005] by <0.1, 0.4, and 0.05, εHf units for reference zircons FC-1, QGNG, and Mudtank, respectively (Table S1). No correlation exists between ^{176}Hf/^{177}Hf and ^{178}Hf/^{177}Hf, ^{174}Hf/^{177}Hf, or ^{176}Lu/^{177}Hf ratios for any zircon reference materials, including the moderate to high Lu/Hf zircons, QGNG, and FC1, indicating that calculations for mass bias and Yb interference corrections were applied accurately. For the unknown zircons, initial ^{176}Hf/^{177}Hf ratios for each spot were calculated using the SHRIMP U-Pb age for the zircon, or when an age for a zircon was not available, the weighted mean average for the rock was used. The initial ^{176}Hf/^{177}Hf ratio refers to the point in time in which the initial melt was removed from the juvenile mantle reservoir and is usually older than the U-Pb zircon age. Present-day chrondritic reservoir (CHUR) compositions of ^{176}Hf/^{177}Hf = 0.282785 ± 11, ^{176}Lu/^{177}Hf = 0.0336 ± 1 [*Bouvier et al*., 2008], and a λ^{176}Lu decay constant of 1.867 ± 8 × 10^{-11} yr^{-1} [*Scherer et al*., 2001; *Söderlund et al*., 2004] were also used to calculate the initial ^{176}Hf/^{177}Hf ratio.

Several sources of uncorrelated error may exist within these LA-MC-ICP-MS analyses that do not account for the external scatter seen in some reference zircons (e.g., Temora-2 and FC1). Therefore, a conservative approach is taken to estimate the absolute uncertainty of each spot that is used to calculate weighted mean εHf compositions. Within-run errors determined for individual zircon analyses are summed in quadrature with an estimate of external reproducibility from the zircon reference materials for each analytical session.

Table 1. Whole-Rock XRF and ICP-MS Data Geochemical Analyses[a]

	ATE01	ATE02	ATE04	ATE05	ATE06
			wt % XRF		
SiO_2	46.66	45.40	46.21	46.59	46.96
TiO_2	1.21	1.23	0.72	1.04	1.20
Al_2O_3	14.07	14.30	15.34	14.25	13.91
Fe_2O_3	12.80	12.17	8.98	10.13	13.06
MnO	0.22	0.21	0.14	0.17	0.21
MgO	8.97	9.62	11.16	10.34	8.42
CaO	12.29	13.09	13.09	11.29	11.82
Na_2O	2.64	2.10	2.06	2.32	2.74
K_2O	0.13	0.03	0.22	0.08	0.10
P_2O_5	0.11	0.11	0.06	0.11	0.10
SO_3	0.01	0.01	0.02	0.01	0.02
LOI	1.25	2.23	2.05	2.17	1.14
Total	100.36	100.50	100.07	98.51	99.68
			ppm ICP-MS		
Rb	3.10	0.70	4.50	1.30	1.20
Ba	109.50	78.50	65.2	105.00	194.50
U	<0.05	0.72	0.33	0.30	0.07
Th	0.19	0.71	0.48	0.50	0.24
Nb	3.40	6.50	1.90	4.40	2.50
Ta	0.30	0.50	0.40	0.50	0.40
La	2.80	7.40	4.40	5.60	2.70
Ce	7.40	19.80	11.20	13.80	8.40
Pr	1.20	3.41	1.67	2.14	1.42
Sr	78.30	145.50	236.00	143.50	64.80
Nd	6.20	16.80	8.70	10.80	7.90
Zr	70.00	69.00	37.00	57.00	59.00
Hf	1.80	1.70	1.10	1.50	1.70
Sm	2.31	5.62	2.44	2.96	2.75
Eu	0.93	2.05	1.08	1.26	1.14
Gd	3.69	6.46	3.07	3.90	4.11
Tb	0.72	0.96	0.55	0.63	0.71
Dy	4.85	5.26	3.38	3.98	4.97
Y	32.30	32.80	20.80	25.00	31.10
Ho	1.13	1.14	0.72	0.88	1.03
Er	3.62	3.48	2.35	2.74	3.41
Tm	0.54	0.54	0.34	0.37	0.48
Yb	3.44	3.47	2.05	2.47	3.19
Lu	0.53	0.54	0.32	0.38	0.49
La_N/Yb_N	0.58	1.53	1.54	1.63	0.61

[a]$Eu = \sqrt{(Sm_N \times Gd_N)}$. N = element normalized to chondrite abundance.

4. Whole-Rock Geochemistry, Petrology, and Mineral Chemistry

4.1. Whole-Rock Geochemistry (Oxide, Trace, and REE)

REE, major and trace element data for five samples from Attunga eclogite are presented in Table 1. Most trace elements are enriched 4 to 10 times relative to primitive mantle reference [*Sun and McDonough*, 1989] (Figure 4). Yb_N/Gd_N ratios demonstrate slight fractionation, with values between 0.58 and 1.63. High variance is seen in all samples amongst the large ion lithophile elements of Ba, Rb, and K, as well as U and Th. This is coupled with small moderate depletion of Ti.

On the Nb/Yb versus Th/Yb plot [*Pearce*, 2008], a slight slab influence is observed with sample ATE04 lying just within the island arc array (Figure 5a). The remaining samples are split between those with strong normal mid-oceanic ridge basalt (N-MORB) ratios and those that plot between N-MORB and continental arc ratios. Ti/V ratios for the Attunga eclogite samples illustrate a suprasubduction zone proximal-MORB setting (Figure 5b). All published Ti and V values from the Weraerai terrane have also been plotted, to demonstrate their suprasubduction setting and their compositional congruence to the Attunga eclogite.

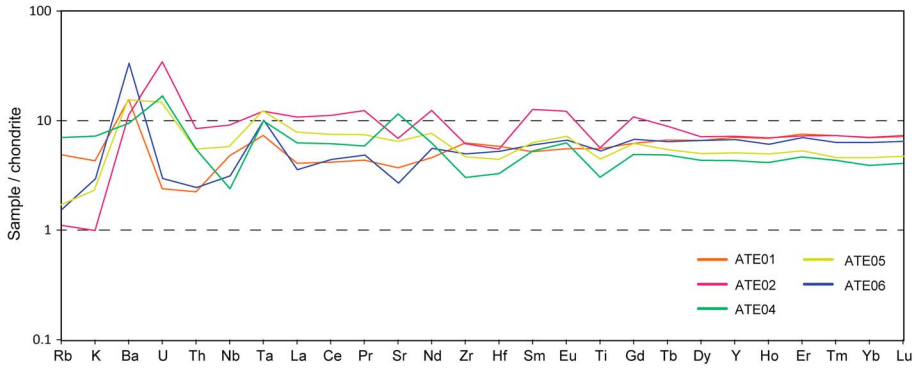

Figure 4. Whole-rock trace element data of samples from the Attunga eclogite. Abundances are normalized with primitive mantle of *Sun and McDonough* [1989].

4.2. Petrology and Major/Trace Element Mineral Chemistry

ATE01 contains abundant (25% by volume) 0.2–1 mm anhedral to subhedral garnet porphyroblasts. All garnets exhibit extensive retrogression to chlorite (Figure 6). Inclusions, as identified by electron microprobe, are mainly albite, quartz, rutile, and epidote. Omphacites occur as large (~500 × 500 μm), subeuhedral to anhedral grains (Figures 6a1 and 6a2) and amphiboles as small fine-grained (30 × 100 μm) clusters and rarer subeuhedral bladed clusters. Tremolitic amphibole is associated with fine-grained albite (50 × 50 μs) and grew under greenschist facies retrogressive conditions (Figures 6b1 and 6b2). This is inferred from their replacement nature around the near-peak metamorphic phases such as garnet and omphacite (Figures 6a1, 6a2, 6c, and 6d1). With the current accepted nomenclature, the samples are described as a retrogressed eclogite as outlined by *Carswell* [1990]. Only a faint orientation within some domains is given by bladed (secondary) tremolitic amphibole that delineates a weak foliation.

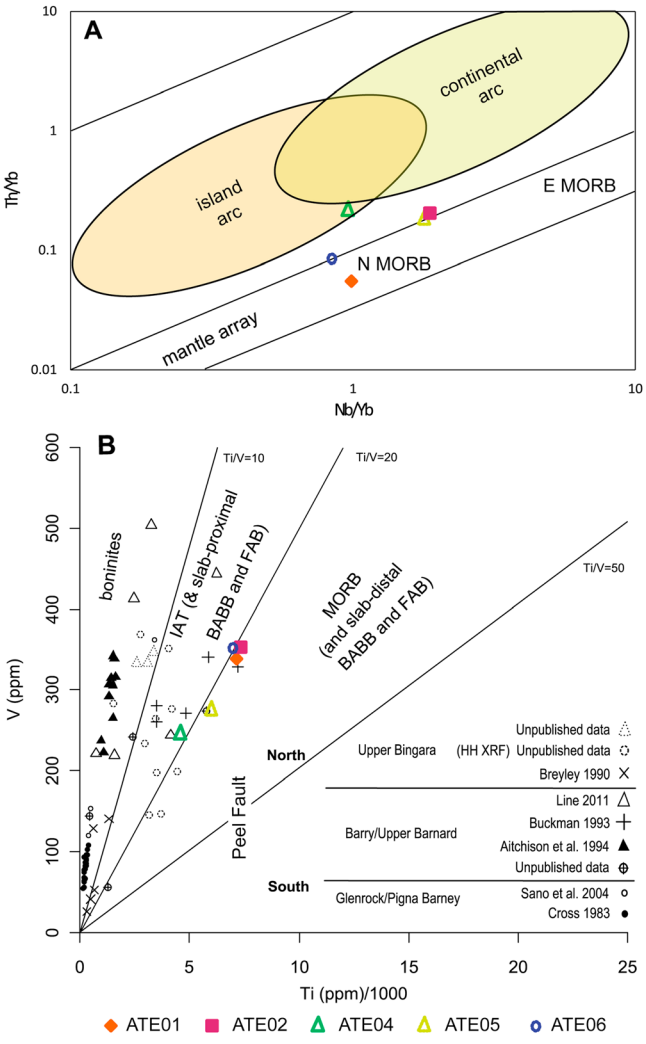

Figure 5. (a) Nb/Yb-Th/Yb diagram [*Pearce*, 2008]. (b) Ti/V plot by *Shervais* [1982]. Attunga eclogite date is circled, and other data are a compilation of geochemical analysis from gabbros/dolerite of the Weraerai terrane.

4.2.1. Garnet

Six garnets were analyzed via electron microprobe. Repeat analysis of garnets AT1a 5, AT1a 6, ATE01 3, and ATE01 4 was undertaken to reproduce trends seen in the core to rim traverses. Garnet ATE01 3 is presented here as a representative example. Grossular content is highest in cores, decreasing to rim. The opposite is observed for pyrope (Figure 7a). Almandine and spessartine decrease toward the rims (Figure 7c), with spessartine exhibiting the classic bell-shaped curve [*Spear*,

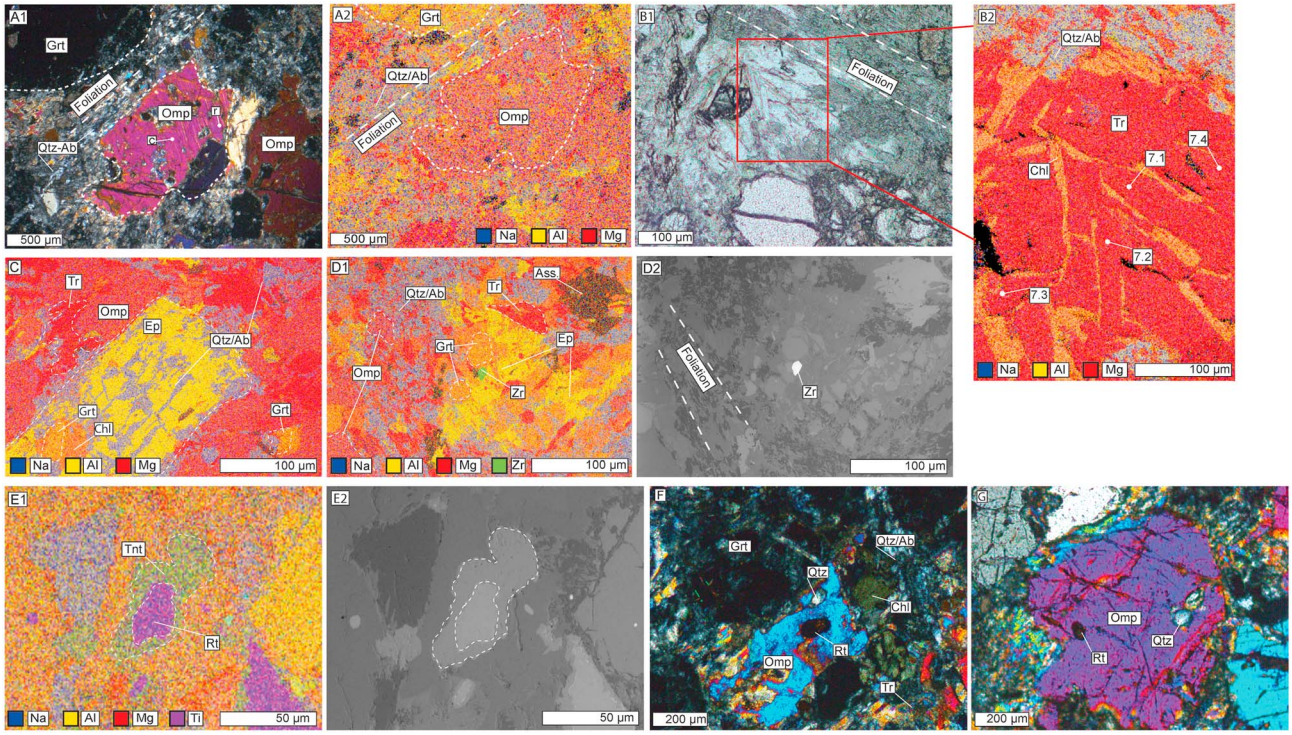

Figure 6. (a1) Cross-polarized light of photomicrograph showing core (c) versus rim (r) microprobe locations for pyroxene ATE1a 3. See Table 1 for data. (a2) Equivalent location represented by energy-dispersive X-ray spectroscopy (EDS) image. Elements analyzed with their respective colors: red: Mg; yellow: Al; and blue; Na. Dark spots are interpreted as accessory phases. This color scheme also applies for Figures 6b2 and 6c. (b1) Plane polarized of image Figure 6b2. (b2) EDS image of bladed tremolitic amphibole, dispersed in fine-grained chlorite groundmass. Numbers refer to microprobe analysis numbers for tremolitic amphibole (tr) in Table 2. (c) EDS image of epidote phenocrysts associated with fine quartz/albite aggregate containing retrogressed garnet. Omphacite retrogressed to tremolitic amphibole and quartz/albite. (d1) Zircon (green) located within garnet retrogressed to chlorite and epidote. (d2) Back-scattered electron image from Figure 6d1, with zircon represented by the bright spot. (e1) Replacement of rutile with titanite forming a corona. Composite image composed of equivalent as previous images, though with Ti: purple. (e2) Outline of rutile (inner) and titanite (outer). (f and g) Omphacitic Na pyroxene with rutile and quartz in inclusions. Mineral abbreviations are as follows: Ab: albite; Tr: tremolitic amphibole; Ass: accessory phases (titanite/zircon/rutile/apatite); Chl: chlorite; Ep: epidote; Grt: garnet; Omp: omphacite; Rt: rutile; and Tnt: titanite.

1993] indicating growth over increasing pressure-temperature (P-T) conditions [*Tomaschek et al*., 2003; *Spandler and Hermann*, 2006]. From core to rim garnet contents are $Alm_{50}Sps_4Prp_{15}Grs_{30}$ to $Alm_{40}Sps_1Prp_{30}Grs_{27}$, respectively (Table 2). Intracrystal fractures, which facilitate retrogression of the garnet to chlorite, are represented by abrupt changes along the cross section (Figure 7c). Analyses which landed on inclusions have also been removed from the transect plots. These compositional variations in Attunga garnets have been documented by *Shaw and Flood* [1974]. Inclusions are more numerous toward the cores relative to the rims and are generally limited to larger garnets (>500 µm). This characteristic has also been noted by *Clarke et al*. [1997], *Spandler and Hermann* [2006], and *Tian and Wei* [2014]. Unlike *Phillips et al*. [2015], we did not find any lawsonite inclusions.

4.2.2. Omphacite

The cores and rims of omphacite are not compositionally distinct (Table 2). In the Ca-Mg-Fe pyroxene versus jadeite versus aegirine diagram of *Morimoto et al*. [1988] the pyroxenes have uniform jadeite (17–23 mol %)-aegirine (4–8 mol %) compositions from core to rim and plot close to, and on, the omphacite-clinopyroxene line (Figure 8a). Estimation of Fe^{3+}/Fe^{2+} is based on stoichiometry and charge balance.

4.2.3. Amphibole

All of the amphiboles are classified as tremolite (ferro-actinolite) using the calcic amphibole scheme of *Hawthorne et al*. [2012]. Tremolitic amphibole is associated with fine-grained quartz-albite groundmass (<50 µm) surrounding omphacite and is clearly retrogressive in origin (Figures 6c, 6d1, and 6d2). It shows a tight clustering of $^{A}(Na + K + 2Ca)$ = 0.04–0.31 pfu (per formula unit) and $^{C}(Al + Fe^{3+}+2Ti)$ = 0.04–0.24 (Figure 8b and Table 3), where ^{A} and ^{C} refer to the idealized cation formula sites for amphibole based on 23 oxygens.

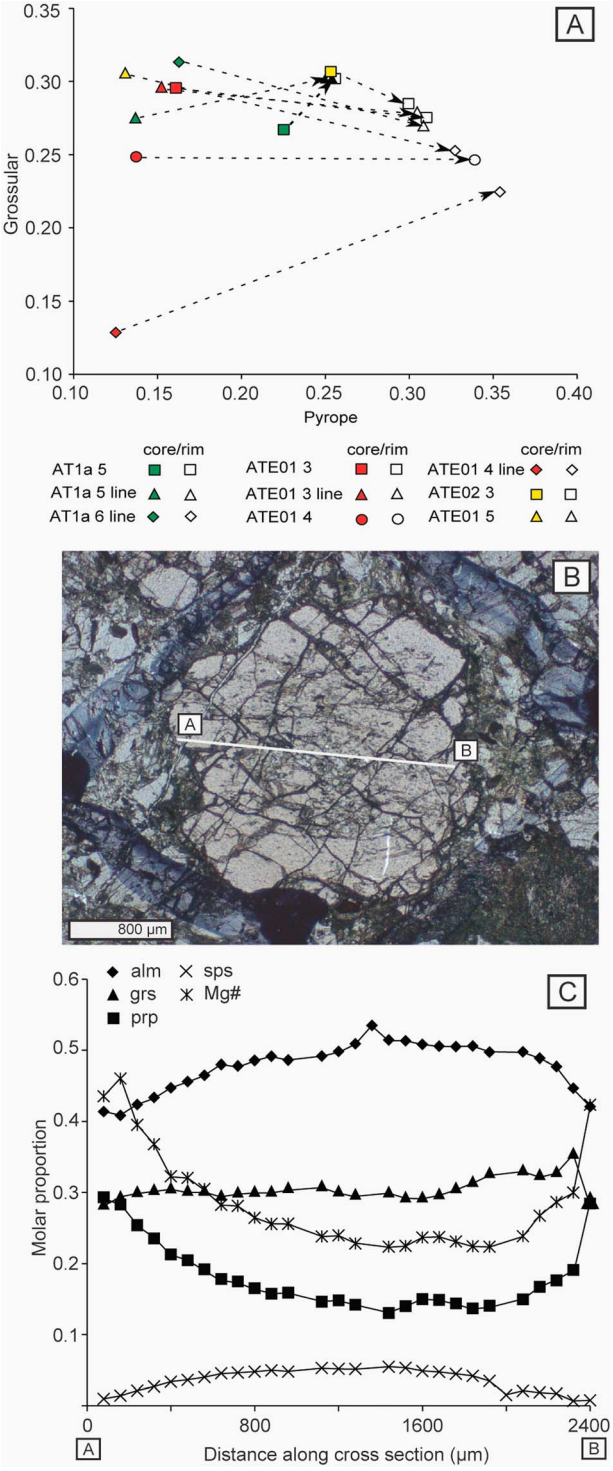

Figure 7. (a)Plot of pyrope versus grossular compositions for core versus rim from garnets. Analysis with "line," have been taken from cross-section profiles, to test reproducibility. (b) Representative garnet cross section, ATE01 3. (c) Molar proportion of Almandine (alm), pyrope (prp), spessartine (sps), grossular (grs), and Mg# = (Mg)/(Mg + Fe^{2+}) for the cross section depicted in Figure 7b. Calculations used for the respective garnet compositions are X_{spess} = Mn/(Fe + Mn + Mg + Ca), X_{alm} = Fe/(Fe + Mn + Mg + Ca), X_{py} = Mg/(Fe + Mn + Mg + Ca), and X_{gross} = Ca/(Fe + Mn + Mg + Ca). Values are mol %, and all Fe is treated as Fe^{2+}. See Table 1 for microprobe results.

4.2.4. Epidote

Epidote occurs as both rare tabular laths (200 × 100 μm) and fine-grained aggregates (10 × 10 μm) throughout much of the sample and as inclusions within the cores of larger garnets. Both generations are closely associated with quartz and albite (Figures 6a1, 6a2, 6d1, and 6d2). $X_{(Fe)}$ values for epidote contained within garnet are tightly clustered, from 0.12 to 0.14, and Ca pfu range from 0.96 to 2.00 (Figure S2 and Table S2).

4.2.5. Rutile/Titanite/Apatite

Rutile occurs as small (~20 μm) grains in the groundmass and as inclusions within garnet and omphacite. In some cases rutile is rimmed by titanite (Figures 6e1 and 6e2). This feature has been as noted by *Clarke et al.* [1997] and *Tian and Wei* [2014] in other high-pressure metamorphic rocks. Titanite rims around rutile are regarded as retrograde decompression features [*Spandler et al.*, 2003; *Spandler and Hermann*, 2006]. Accessory apatite and zircon are present (Figures 6d1 and 6d2).

5. SHRIMP U-Pb Zircon Geochronology

5.1. Zircon Petrography

After reconnaissance CL imaging prior to the U-Pb dating, high-resolution CL imagery was carried out at the Wollongong University Innovation Campus. Images were recorded in blue, rather than white light, in order to reduce "noise" created by red light. There are three distinct types of zircon, which we term types I, II, and III (Figure 9). Type I zircons are dull to dark in CL, form cores, and are typically devoid of observable structure. This is only observed in 8 of approximately 100 mounted zircons. Type II zircon domains are the dominant textural type and are characterized by an increase in the CL signal (brightness). Ghost zoning, whereby partial recrystallization occurs, is apparent in many of these

Table 2. Selected Microprobe Analysis of Garnet and Pyroxene[a]

Sample/Garnet	AT1a 5		AT1a 6	ATE01 3	ATE01 4			ATE1a 3		ATE01 7		ATE01 8		ATE02 2	
Mineral	g-c	g-r	g-c	g-c	g-r	g-c	g-r	o-c	o-r	o-c	o-r	o-c	o-r	o-c	o-r
SiO_2	38.42	38.93	37.93	38.01	39.09	37.84	39.19	52.81	52.33	52.21	53.04	52.86	52.65	52.83	52.96
TiO_2	0.12	0.16	0.20	0.14	0.10	0.09	0.05	0.29	0.33	0.30	0.33	0.34	0.32	0.33	0.31
Al_2O_3	21.80	21.75	21.39	21.38	21.87	21.27	22.05	8.51	8.54	7.84	7.84	8.47	8.23	7.84	7.88
Cr_2O_3	bdl	bdl	bdl	bdl	bdl	bdl	0.04	bdl	bdl	bdl	bdl	bdl	bdl	bdl	bdl
FeO	22.69	20.85	23.97	23.49	20.22	26.01	20.33	4.78	4.74	4.93	4.73	4.68	4.75	4.83	4.91
MnO	bdl	bdl	0.63	1.91	0.44	2.05	0.33	0.00	0.00	0.00	0.00	0.00	0.00	0.05	0.00
MgO	5.88	6.63	3.93	4.14	8.09	3.58	8.89	10.86	11.01	11.40	11.65	11.38	11.33	11.56	11.44
CaO	10.16	11.59	12.02	11.08	10.75	8.99	9.65	18.25	18.47	19.17	19.43	18.99	19.15	19.35	19.36
Na_2O	0.04	0.06	0.07	0.05	0.04	0.05	bdl	3.69	3.73	3.20	3.19	3.35	3.47	3.35	3.21
K_2O	bdl	bdl	bdl	bdl	bdl	bdl	bdl	bdl	bdl	bdl	bdl	bdl	bdl	bdl	bdl
Total	99.11	99.97	100.14	100.20	100.60	99.88	100.53	99.19	99.15	99.05	100.21	100.07	99.90	100.14	100.07
O	12	12	12	12	12	12	12	6	6	6	6	6	6	6	6
Si	2.96	2.97	2.96	2.96	2.96	2.98	2.96	1.92	1.90	1.91	1.91	1.91	1.90	1.91	1.92
Ti	0.01	0.01	0.01	0.01	0.01	0.00	0.01	0.01	0.01	0.01	0.01	0.01	0.01	0.01	0.01
Al	1.98	1.95	1.97	1.97	1.95	1.98	1.95	0.36	0.37	0.34	0.33	0.36	0.35	0.33	0.34
Cr	0.00	0.00	0.00	0.00	0.00	0.00	0.00	0.00	0.00	0.00	0.00	0.00	0.00	0.00	0.00
Fe^{3+}	0.10	0.10	0.10	0.09	0.13	0.04	0.13	0.04	0.07	0.06	0.04	0.04	0.07	0.07	0.04
Fe^{2+}	1.36	1.23	1.47	1.44	1.15	1.67	1.15	0.11	0.07	0.09	0.10	0.10	0.07	0.08	0.11
Mn	0.09	0.05	0.04	0.13	0.03	0.14	0.03	0.00	0.00	0.00	0.00	0.00	0.00	0.00	0.00
Mg	0.67	0.75	0.46	0.48	0.91	0.42	0.91	0.59	0.60	0.62	0.63	0.61	0.61	0.62	0.62
Ca	0.84	0.95	1.00	0.93	0.87	0.76	0.87	0.71	0.72	0.75	0.75	0.73	0.74	0.75	0.75
Na	0.00	0.00	0.00	0.00	0.00	0.00	0.00	0.26	0.26	0.23	0.22	0.23	0.24	0.23	0.23
K	0.00	0.00	0.00	0.00	0.00	0.00	0.00	0.00	0.00	0.00	0.00	0.00	0.00	0.00	0.00
Sodic and Calcic Clinopyroxene End-members mol %															
almandine	48.05	39.51	49.39	48.45	38.85	55.90	39.16	Aegerine	3.83	7.60	6.10	4.53	4.10	7.14	7.20	4.30
pyrope	13.00	32.73	15.39	16.15	30.81	14.09	33.78	Jadeite	22.96	19.17	17.10	18.37	20.10	17.55	16.66	18.78
grossular	30.56	25.28	32.05	29.65	27.52	24.82	24.77	Diopside	73.21	73.24	76.80	77.10	75.80	75.31	76.15	76.92
spessartine	6.96	0.84	1.41	4.25	0.95	4.59	0.70									
Ortho and Calcic Clinopyroxene End-members mol %															
								Wo	50.50	51.92	51.31	50.88	50.71	52.03	51.77	50.91
								En	41.81	43.06	42.46	42.44	42.28	42.83	43.03	41.86
								Fs	7.69	5.01	6.23	6.68	7.01	5.14	5.19	7.24

[a]bdl: below level of detection ~0.01%; c, core; r, rim. Total FeO is reported as FeO. Pyroxene nomenclature is from *Morimoto et al.* [1988].

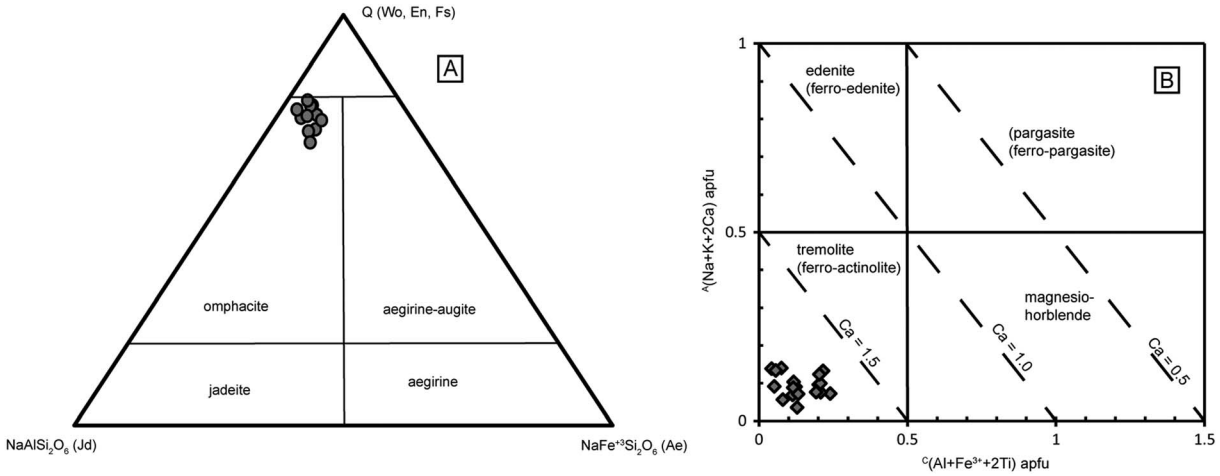

Figure 8. (a) Clinopyroxene classification scheme after *Morimoto et al.* [1988]. Normalization conducted to 6 oxygen and 4 cations. (b) Calcic amphibole classification scheme, from *Hawthorne et al.* [2012]. Oxidation state of iron and cation site distribution is calculated on the basis of charge balance.

Table 3. Selected Microprobe Analysis of Amphiboles[a]

Sample	ATE1a				ATE02													
Spot	7.1	7.2	7.3	7.4	1.1	2.1	2.2	2.3	3.1	3.2	3.3	4.3	5.1	5.2	6.1	6.2	6.3	6.4
Mineral	Tr	Tr	Tr	Tr	Tr	Tr	Tr	Tr	Tr	Tr	Tr	Tr	Tr	Tr	Tr	Tr	Tr	Tr
SIO_2	54.28	54.57	54.8	54.64	55.18	53.51	55.54	55.06	52.94	54.21	54.36	54.37	53.83	53.41	53.34	53.86	52.62	53.39
TiO_2	0	0	0.01	0	bd	bd	bd	bd	bd	bd	bd	bd	bd	bd	bd	bd	bd	bd
Al_2O_3	1.02	1.23	1.26	1.14	1.26	0.42	0.72	0.58	1.45	0.85	0.8	0.81	0.39	1.39	0.66	0.78	0.68	0.81
Cr_2O_3	bd	bd	bd	bd	bd	bd	bd	bd	bd	bd	bd	bd	bd	bd	bd	bd	bd	bd
FeO	12.84	11.18	11.11	11.45	10.81	11.33	9.65	11.39	11.08	11.47	11.46	13.16	11.79	11.08	12.14	13.34	12.64	12.65
MnO	0.23	0.06	0.1	0.14	0.1	0.13	0.09	0.17	0.13	0.14	0.18	0.22	0.17	0.09	0.14	0.21	0.14	0.24
MgO	15.71	16.82	17.09	16.39	16.97	16.62	17.82	16.94	16.26	16.28	16.3	15.5	16.15	16.22	15.75	15.21	15.41	15.2
CaO	11.59	11.68	11.67	11.5	11.57	12.3	12.27	12.18	11.31	11.87	11.81	11.42	12.08	11.32	12.06	11.92	12	11.69
Na_2O	0.84	0.87	0.83	0.9	1.07	0.43	0.49	0.53	1	0.76	0.8	0.85	0.44	1.05	0.72	0.62	0.62	0.58
K_2O	0.1	0.07	bd	0.05	bd	bd	bd	0.09	0.08	0	0.09	0.08	0	0.05	0.05	0.08	0.06	0.14
Total	96.61	96.48	96.87	96.21	96.96	94.74	96.58	96.94	94.25	95.58	95.8	96.41	94.85	94.61	94.86	96.02	94.17	94.7
O	23	23	23	23	23	23	23	23	23	23	23	23	23	23	23	23	23	23
T Si	7.90	7.86	7.85	7.90	7.89	7.89	7.94	7.91	7.82	7.91	7.92	7.91	7.93	7.86	7.90	7.90	7.87	7.92
T Al	0.10	0.14	0.15	0.10	0.11	0.07	0.06	0.09	0.18	0.09	0.08	0.09	0.07	0.14	0.10	0.10	0.12	0.08
C Al	0.08	0.07	0.06	0.10	0.11		0.06	0.01	0.07	0.06	0.06	0.05	0.00	0.10	0.01	0.04		0.06
C Fe^{3+}	0.00	0.13	0.18	0.11	0.10	0.05	0.07	0.10	0.14	0.07	0.06	0.14	0.08	0.11	0.03	0.08	0.06	0.07
C Mg	3.41	3.61	3.65	3.53	3.62	3.65	3.80	3.63	3.58	3.54	3.54	3.36	3.55	3.56	3.48	3.33	3.44	3.36
C Fe^{2+}	1.52	1.19	1.11	1.26	1.18	1.30	1.07	1.26	1.20	1.33	1.34	1.45	1.37	1.24	1.47	1.56	1.51	1.50
C Mn^{2+}	0.00	0.00	0.00	0.00	0.00	0.00	0.00	0.00	0.00	0.00	0.01	0.00	0.00	0.00	0.01	0.00	0.00	0.01
B Fe^{2+}	0.05	0.03	0.04	0.02	0.02	0.01	0.01	0.01	0.02	0.00	0.00	0.01	0.00	0.02	0.00	0.00	0.00	0.00
B Mn^{2+}	0.03	0.01	0.01	0.02	0.01	0.02	0.01	0.02	0.02	0.02	0.02	0.03	0.02	0.01	0.01	0.02	0.02	0.02
B Ca	1.81	1.80	1.79	1.78	1.77	1.94	1.88	1.88	1.79	1.86	1.84	1.78	1.91	1.78	1.91	1.87	1.92	1.86
B Na	0.12	0.16	0.16	0.19	0.20	0.03	0.10	0.10	0.17	0.13	0.14	0.18	0.07	0.19	0.08	0.10	0.06	0.12
A Na	0.12	0.08	0.07	0.07	0.10	0.09	0.04	0.05	0.12	0.09	0.09	0.06	0.06	0.11	0.13	0.07	0.12	0.05
A K	0.02	0.01	0.00	0.01	0.00	0.00	0.00	0.02	0.02	0.00	0.02	0.02	0.00	0.01	0.01	0.02	0.01	0.03
Sum	15.14	15.10	15.07	15.08	15.10	15.05	15.04	15.07	15.13	15.09	15.11	15.08	15.06	15.12	15.14	15.09	15.12	15.07
x(Fe)	0.69	0.75	0.77	0.74	7.89	7.89	7.94	7.91	7.82	7.91	7.92	0.70	0.72	0.74	0.70	0.68	0.69	0.69

[a] $x(Fe) = Mg/(Mg + Fe^{2+})$.

type II zircons. Type III zircon is largely homogeneous and has a slightly duller CL signal relative to II (Figure 9a). Type III zircon is always located to the edge of grains, with thicker portions on the broadest ends of grains. Type III zircon is generally 10–20 μm broad as rims and in three cases, up to 50 μm. The boundary between type II and type III zircon is sharp and lobate in nature with the type III outside rim having a spongy texture (Figure 9d).

5.2. Zircon U-Th-Pb

All analyzed zircons, with their respective spot locations, are illustrated in Figure 10. Six analyses are of type I zircon domains of dull to dark CL signatures, and 15 are on bright type II zircon domains. Type III zircon rims were too narrow to be analyzed. Analyses of type II zircon from ATE01 have low U content, all with <50 ppm and most with <2 ppm, and have Th/U ratios of <0.1 (Table 4). The type I cores have higher U abundance (up to 294 ppm) with high Th/U ratios of 0.37 to >1.0. In some of the very low U abundance type II zircons there is an appreciable proportion of common Pb in the analyses (*f*206 > 2% in Table 4; where *f*206 is the percentage of ^{206}Pb of nonradiogenic origin), simply because of the small amount of radiogenic Pb that has been produced in the past half billion years.

Low abundances of U, Th, and radiogenic Pb in type II zircon resulted in large analytical errors. The data are presented *uncorrected* for common Pb in a Tera-Wasserburg $^{238}U/^{206}Pb$-$^{207}Pb/^{206}Pb$ concordia diagram (crosses in Figure 11a). Regression of this data gives rise to a lower Concordia intercept of 490 ± 14 Ma (mean square weighted deviate (MSWD) = 0.43) which is the radiogenic U-Pb component interpreted as giving the age of type II zircons (the intercept of the regression line with the $^{207}Pb/^{206}Pb$ axis gives the $^{207}Pb/^{206}Pb$ isotopic ratio of the common Pb). Another assessment of the age of these zircons is based on $^{238}U/^{206}Pb$ following correction for common Pb using the 207 correction method (which assumes concordancy) [*Compston et al.*, 1984]. Using analyses with <2% *f*206, this gives a weighted mean $^{238}U/^{206}Pb$ age of

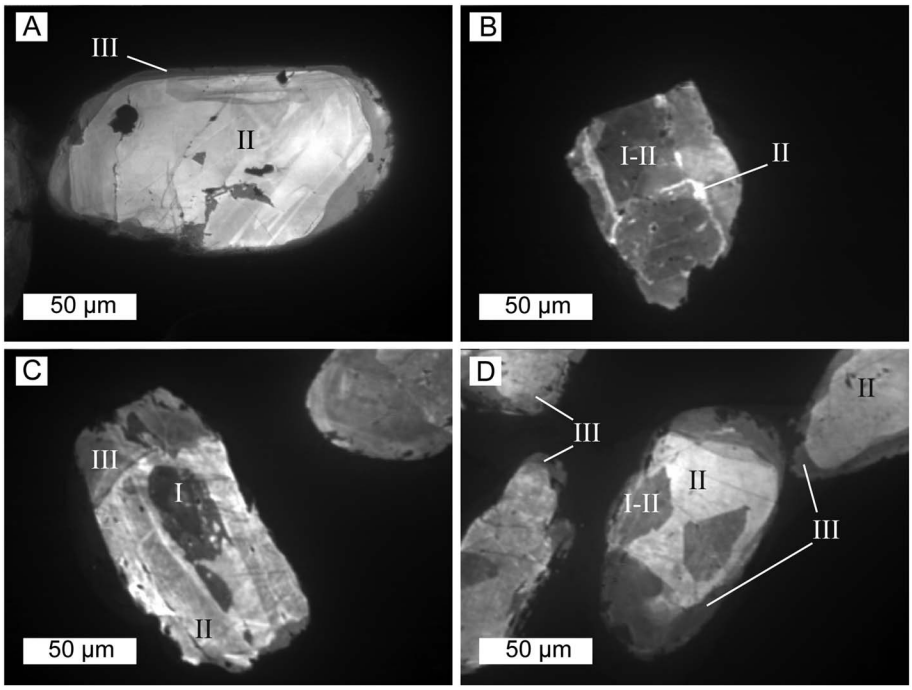

Figure 9. Panchromatic images of represented zircon. Four types zircon morphology are described. Type I: dark CL, high REE contents (>600), and Th/U ratios between 0.4 and 1.0. Type II: zoning is brighter and lacks magmatic oscillatory zoning; REE content is less than 150. Type III occur as rims, bright-dull homogenous CL signal. Analyses are not carried out on this zircon type.

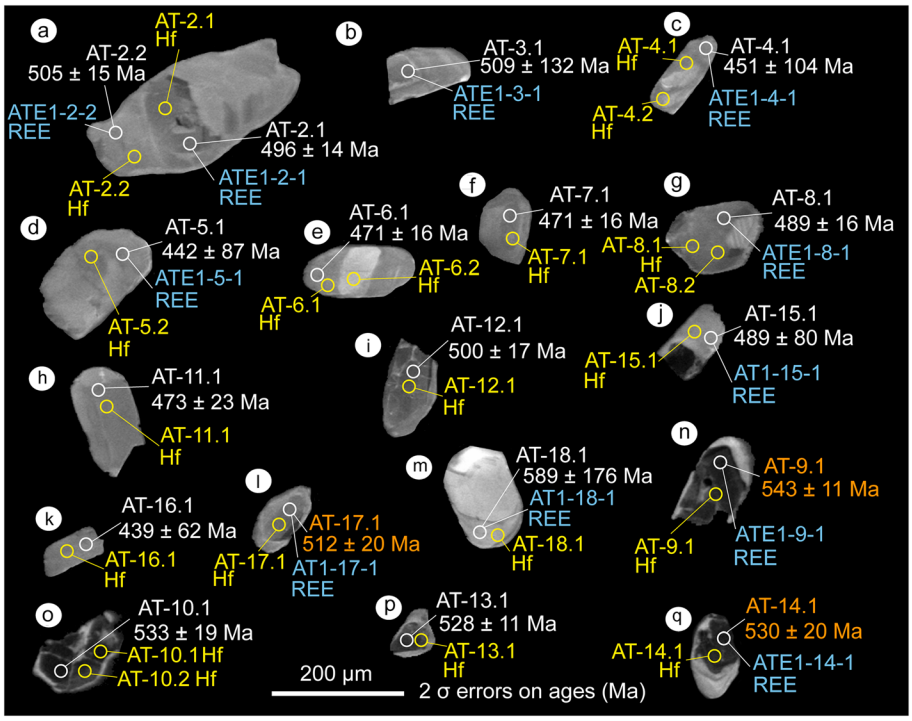

Figure 10. Cathodoluminescence images of zircons extracted from Attunga eclogite showing dominantly bright, recrystallized metamorphic zircons with the occasional darker, oscillatory zoned inherited igneous core. White: U-Pb SHRIMP analysis; blue: LA-ICP-MS, REE analysis; and yellow: LA-ICP-MS, Lu-Hf analyses. Red text refers to the 534 ± 14 Ma U-Pb age population based on weighted mean average.

Table 4. Summary SHRIMP Zircon U-Th-Pb Data[a]

Labels	Zircon Type	Grain	U/ppm	Th/ppm	Th/U	$^{204}Pb/^{206}Pb$ Ratio	Common ^{206}Pb%	$^{238}U/^{206}Pb$	$^{207}Pb/^{206}Pb$	Age* $^{238}U/^{206}Pb$
2.1	II	e, h, and p	34	0.78	0.023	<0.00001 ± 0.00019	<0.001	12.324 ± 0.373	0.0551 ± 0.0015	505.1 ± 14.7
2.2	II	m, h, and p	48	1.14	0.024	0.00018 ± 00015	<0.001	12.512 ± 0.373	0.0575 ± 0.0020	496.5 ± 14.3
2.3	II	e, h, and p	11	0.21	0.019	0.00175 ± 0.00092	0.538	12.963 ± 0.530	0.0640 ± 0.0029	476.6 ± 18.9
2.4	II	m, hd, and p	40	0.79	0.020	0.00056 ± 0.00022	<0.001	12.930 ± 0.604	0.0583 ± 0.0023	480.7 ± 21.7
3.1	II	e, h, and p	0.4	0.01	0.014	0.05990 ± 0.02791	7.332	11.274 ± 2.991	0.1253 ± 0.0291	509.2 ± 132.4
4.1	II	m, h, and p	1.2	0.09	0.076	0.03104 ± 0.01390	4.730	13.124 ± 3.089	0.1018 ± 0.0176	451.8 ± 103.9
5.1	II	e, h, and p	1.3	0.03	0.028	<0.00001 ± 0.00467	2.584	13.729 ± 1.500	0.0825 ± 0.0121	441.9 ± 47.2
5.2	II	m, hd, and p	1.0	0.06	0.060	0.01646 ± 0.01425	0.511	10.992 ± 1.605	0.0637 ± 0.0157	558.5 ± 79.1
6.1	II	e, h, and p	0.7	0.03	0.040	0.08182 ± 0.02821	8.214	11.034 ± 1.883	0.1333 ± 0.0250	515.1 ± 86.4
7.1	II	e, h, and p	1.0	0.04	0.042	0.00703 ± 0.00494	2.948	12.787 ± 2.417	0.0858 ± 0.0242	471.6 ± 87.5
8.1	II	m, h, and p	35	1.96	0.056	<0.00001 ± 0.00010	<0.001	12.726 ± 0.429	0.0557 ± 0.0021	489.4 ± 15.9
9.1	I	c, h, and p	293	108	0.369	0.00013 ± 0.00009	<0.001	11.372 ± 0.242	0.0588 ± 0.0007	543.5 ± 11.1
10.1	I	c, h, and p	263	312	1.186	<0.00001 ± 0.00004	0.028	11.600 ± 0.432	0.0594 ± 0.0007	532.9 ± 19.1
11.1	II	e, h, p, and fr	9	0.01	0.001	0.00253 ± 0.00131	0.533	13.064 ± 0.671	0.0640 ± 0.0037	473.0 ± 23.5
12.1	II	c, hd, p, and fr**	64	48	0.753	0.00034 ± 0.00019	<0.001	12.402 ± 0.442	0.0584 ± 0.0011	500.3 ± 17.2
13.1	I	c, hd, and eq	166	109	0.654	0.00017 ± 0.00008	<0.001	11.745 ± 0.393	0.0575 ± 0.0011	527.7 ± 17.0
14.1	I	c, hd, p, and fr	214	168	0.787	0.00013 ± 0.00005	<0.001	11.694 ± 0.518	0.0576 ± 0.0006	529.8 ± 22.6
15.1	II	r, h, p, and fr	0.8	0.25	0.336	0.02440 ± 0.01279	0.972	12.329 ± 2.054	0.0679 ± 0.0145	498.0 ± 80.7
16.1	II	e, h, and p	1.0	0.05	0.048	0.00475 ± 0.00438	2.524	13.821 ± 1.977	0.0819 ± 0.0186	439.3 ± 61.7
17.1	I	c, h, and p	54	30	0.562	0.00040 ± 0.00019	0.142	12.073 ± 0.499	0.0604 ± 0.0023	512.3 ± 20.4
18.1	II	r, h, and p	0.4	0.02	0.070	0.01748 ± 0.01771	10.927	9.312 ± 2.848	0.1578 ± 0.0301	588.9 ± 175.8

[a]The two types of zircon morphology analyzed are type I and type II. Labels: *x*, *y* = grain *x*, analysis *y*. Analysis 1.1 abandoned because U, Th, and Pb abundance is too low for peak centering p = prismatic, eq = equant, e = end, m = middle, r = overgrowth, c = core, h = homogeneous and sector zoning, hd = homogeneous dark, and fr = fragment.

*Age corrected for common Pb by the 207 method and 500 Ma model Pb of *Cumming and Richards* [1975]. All errors are to 1σ.

**Analysis is composite, core targeted, but overlaps onto rim analytical errors that are given at the 1σ level U-Pb isotopic ratios given prior to correction for common Pb.

492 ± 13 Ma (MSWD = 0.33), indistinguishable from the regression treatment of the data *not* corrected for common Pb and with no assumption about the common Pb composition.

The analyses of the type I zircon cores with higher U abundance have lower proportions of common Pb and yield close to concordant ages, even prior to correction for common Pb (ovals in Figures 11a and 11b). Rejecting analysis 12.1 which might have lost small amounts of radiogenic Pb, the remaining five analyses yield a weighted mean $^{238}U/^{206}Pb$ age of 534 ± 14 Ma (MSWD = 0.51; data corrected for common Pb by the 207 correction method).

6. LA-ICP-MS Zircon and Garnet Trace Element Chemistry

6.1. Zircon Rare Earth Element Chemistry

REE data are presented in Table 5 and illustrated in a chondrite-normalized plot (Figure 12). Type I zircons have higher ΣREE contents, 656.5 to 972.8, whereas type II zircons have lower values of 9.2 to 222.7, with a median of 49. Type I zircons have chondrite-normalized Lu values >2000, with depletion of La to subchondritic values, negative Eu anomalies ($Eu^a = Eu_N/\sqrt{(Sm_N \times Gd_N)}$ of 0.13 to 0.28 and positive Ce anomalies. The low Th/U type II zircon shows different REE abundances. In many of the analyses the light REEs apart from Ce are below level of detection, whereas Lu occurs at 862 down to 23 times chondrite abundance, i.e., considerably less than the >2000 of type I zircon. Anomalous high ΣREE values within type II zircon is found with two analysis, ATE1-4-1 (ΣREE = 141.4) and ATE1-8-1 (ΣREE = 222.7) (Table 5). With one exception, analyses of type II zircon show negligible Eu anomalies. The anomalous analysis 8.1 (Figure 10g, zircon) shows modest depletion in the HREE relative to type I zircon, a negative Eu anomaly, and a higher U content than most of the other type II zircons (Tables 4 and 5 and Figure 12). This analysis was on the edge of the zircon grain (Figure 10) and does not appear to contain type I core zircon, to explain the negative Eu anomaly. For type II zircon a weak positive collation exists between Yb_N/Gd_N and the corrected U-Pb zircon age (R^2 = 0.65) (Figure 13b). Thus, the type II zircons, with apparently marginally older U-Pb ages (but still within analytical error), have higher HREE content.

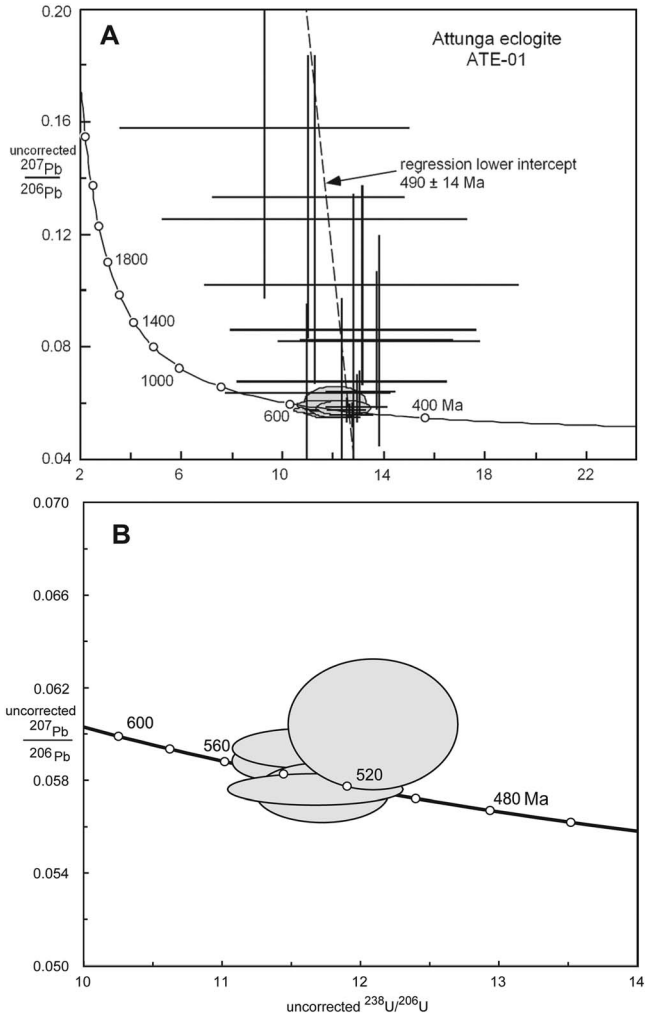

Figure 11. Tera-Wasserburg plot ($^{238}U/^{206}Pb$–$^{207}Pb/^{206}Pb$). (a) Crosses depict recrystallized zircon, gray ovals represent igneous zircon. (b) Enlarged view of the concordant igneous zircons. Data uncorrected for common Pb and analytical errors depicted at the 2σ level.

6.2. Garnet Rare Earth Element Chemistry

Garnet cores are characterized by HREE enrichment La_N/Dy_N = 5–30, average = 18 with negligible Eu anomalies Eu/Eu^a = 1.40–0.55. This garnet type is restricted to larger (<500 μm) inclusion rich cores. Only 3 of the 19 analyses are represented by this garnet type with the most extreme HREE values represented by garnet core 1.5 (Figure 14a and Table 6). The cores of smaller inclusion-free garnets (<75 μm) differ substantially from their larger counterparts. They are classified as "mantle" type meaning the cores of small garnets. This rule does not apply to garnet 6, which has diameter of ~200 μm and a core which has similar geochemical affinities to smaller mantle garnets. A clear distinction is observed from core to mantle HREE contents based on a ratio to their respective rims. With $(La_N/Dy_{N\ core})/(La_N/Dy_{N\ rim})$ avg = 22.02 and $(La_N/Dy_{N\ mantle})/(La_N/Dy_{N\ rim})$ avg = 1.87. All garnet rims have flat to concave down HREE patters (Figure 14a) with La_N/Dy_N = 3.31–0.23 and no Eu anomalies (Eu/Eu^a avg = 0.98).

Trace element partition coefficients were calculated between zircon and garnet core, mantle, and rim. Strong partitioning of Ho-La (Figure 14b and Table 7) into type II zircon relative to garnet rims is demonstrated by the Lu/Dy coefficient ratio ($(La/Dy)_{Dzr/grt\ rim}$) = 8.53. Zircon versus garnet mantle is lower at $(La/Dy)_{Dzr/grt\ mantle}$ = 4.35, and the lowest partition coefficients are seen between zircon and garnet core, $(La/Dy)_{Dzr/grt\ core}$ = 0.76.

6.3. Ti-in-Zircon Thermometry

Titanium and other trace element concentrations were acquired via LA-ICP-MS at the same time as the REE (Table 5). Some of the analyses show high Ti content (>20 ppm), which coupled with higher Ca, P, or Y abundances suggests that micron-scale inclusion phases have contributed to the analyses. Therefore, discussion of Ti-in-zircon abundance is restricted to analyses of metamorphic zircon where the low abundance of other elements such as Ca suggests that the Ti is present in the zircon, not partially in inclusion phases. For these sites Ti abundance is well beyond analytical error from 9.4 to 2.8 ppm (Table 5).

The temperature of zircon crystallization can be established by the Ti concentration of zircon in equilibrium with rutile and quartz [*Watson and Harrison*, 2005], a criterion met by the Attunga metamorphic zircons. Using the *Ferry and Watson* [2007] recalibration of this thermometer ($\log(Ti\ ppm) = 5.711–4800/T - \log(aSiO_2) + \log(aTiO_2)$, with T = temperature in kelvins), temperatures range from 612 ± 7 to 770 ± 8°C, suggesting eclogite zircon crystallization over an ~160°C range (Figure 13A2).

AGU Tectonics

10.1002/2016TC004408

Table 5. LA-ICP-MS Zircon Rare Earth Element Analyses

Labels	Unit of Measurement	ATE1-2-1	ATE1-2-2	ATE1-3-1	ATE1-4-1	ATE1-5-1	ATE1-8-1	ATE1-9-1	ATE1-14-1	ATE1-15-1	ATE1-17-1	ATE1-18-1	ATE1-18-2	ATE1-19-1
Site		r,h,p	c,h,p	c,osc,fr	r,h,pr	r,h,pr	r,h,p	m,hd,fr	c,sz,fr	r,rex,fr	m,h,ov	r,h,pr	r,h,pr	
La	ppm	0.00	0.01	0.00	0.00	0.00	0.00	0.01	0.01	0.00	0.00	0.00	0.00	0.00
Ce	ppm	0.01	0.05	0.00	0.12	0.01	0.18	1.47	2.71	0.01	1.55	0.01	0.00	1.31
Pr	ppm	0.00	0.00	0.00	0.01	0.00	0.00	0.04	0.05	0.00	0.05	0.00	0.15	0.07
Nd	ppm	0.01	0.10	0.01	0.10	0.03	0.07	0.53	0.64	0.01	1.10	0.00	0.01	1.52
Sm	ppm	0.02	0.11	0.01	0.28	0.01	0.34	1.37	1.51	0.01	2.96	0.02	0.01	3.81
Eu	ppm	0.02	0.10	0.00	0.10	0.02	0.22	0.25	0.18	0.01	0.50	0.01	0.01	0.90
Gd	ppm	0.27	0.99	0.05	2.92	0.21	3.23	10.25	11.97	0.16	20.58	0.14	0.06	25.03
Tb	ppm	0.14	0.46	0.05	1.07	0.12	1.40	3.94	4.44	0.12	6.80	0.08	0.06	8.68
Dy	ppm	2.88	7.20	0.92	16.16	2.02	22.88	61.12	69.16	2.43	93.28	2.52	1.72	121.73
Ho	ppm	1.44	3.16	0.48	6.35	0.70	9.42	25.80	29.42	1.27	35.65	1.50	1.17	46.41
Er	ppm	8.84	16.58	2.63	30.93	2.97	47.41	138.13	156.28	7.29	171.61	10.84	8.90	222.22
Tm	ppm	2.14	3.64	0.48	6.58	0.52	10.33	31.27	35.58	1.62	34.95	2.95	2.50	44.69
Yb	ppm	24.58	38.31	4.03	64.44	4.35	105.35	320.29	365.31	15.82	325.54	31.45	28.53	418.19
Lu	ppm	5.36	7.62	0.58	12.39	0.66	21.90	62.29	75.23	2.70	61.76	5.46	6.00	78.21
Th	ppm	0.16	0.72	<0.00	1.15	0.02	2.20	78.47	200.92	0.16	10.86	0.03	0.00	6.61
Ta	ppm	0.07	0.08	0.04	0.12	0.05	0.07	0.35	0.82	0.04	0.28	0.12	0.09	0.52
Nb	ppm	0.71	0.672	0.511	0.777	0.585	0.709	1.113	1.784	0.513	1.034	0.561	0.689	1.37
Ti	ppm	2.8 ± 0.16	5.47 ± 0.37	1.85 ± 0.19	13.79 ± 0.77	8.35 ± 0.32	3.62	8.28	115.75	4.85 ± 0.27	53.73	3.15 ± 0.29	3.71 ± 0.2	9.35 ± 0.35
Ca	ppm	<15.83	82.05	<18.88	29.08	<13.12	<14.54	<13.98	362.41	<18.59	186.23	12.09	<18.54	<18.32
Y	ppm	53.45	110.61	19.34	193.08	25.15	333.39	920.72	1077.04	45.72	1154.42	56.84	48.71	1467.77
P	ppm	51.29	54.62	43.38	67.12	42.7	103.97	218.86	208.85	45.05	198.26	35.96	42.76	258.29
Eu/Eu[a]		0.66	0.88	0.64	0.34	1.10	0.64	0.20	0.13	0.56	0.19	0.58	0.83	0.28
Ti-in-zircon	temperature °C	640 ± 6	691 ± 7	612 ± 7	770 ± 8	725 ± 7	659 ± 6			681 ± 6		649 ± 7	661 ± 6	725 ± 7
Yb_N/Gd_N[b]		114.2	47.7	103.8	27.3	25.1	40.3	38.6	37.7	123.0	19.6	277.7	555.3	20.7
ΣREE[c]	ppm	45.7	78.3	9.2	141.4	11.6	222.7	656.8	752.5	31.5	756.3	55.0	49.1	972.8
Zircon type		II	II	II	II	II	II	I	I	II	I	II	II	II

[a] $Eu = \sqrt{(Sm_N \times Gd_N)}$.
[b] N = element normalized to chondrite.
[c] ΣREE = sum of all REE.

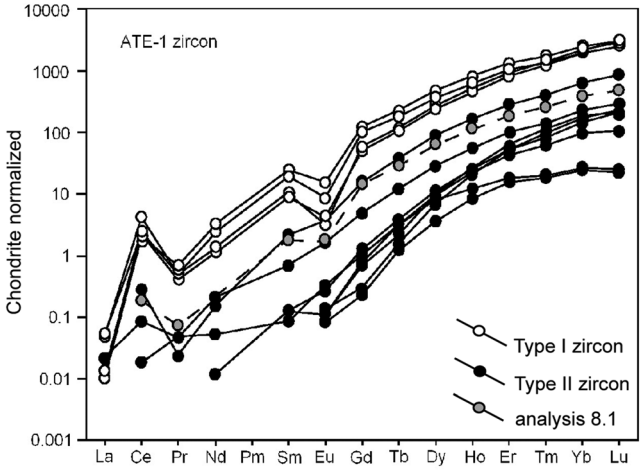

Figure 12. Chondrite-normalized [*Sun and McDonough*, 1989] plot of zircon REE LA-ICP-MS analyses.

6.4. Zircon Hf Isotopic Data

All of the initial $^{176}Lu/^{177}Hf$ measured in the Attunga zircon have ratios lower than 0.003. Twenty-seven Lu-Hf analyses are undertaken on 22 ATE01 zircons (Table 8). $\varepsilon Hf_{(0)}$ *(present-day)* values range from +17.5 to −6.0, with $\varepsilon Hf_{(t)}$ up to +17.7 (Figure 15). Most of the $\varepsilon Hf_{(t)}$ values are $>$ +10, with an weighted mean average of 13.5 ± 0.8, congruent with estimates of contemporaneous depleted mantle compositions. This is further illustrated by depleted mantle model ages (Table 8), which range from ~710 to ~460 Ma, equal to or in some cases slightly older than U-Pb zircon ages.

7. Discussion and Interpretations

7.1. Protolith Characteristics for the Attunga Eclogite

Shaw and Flood [1974] describe the Attunga eclogite as derived from ocean floor basalt, based on the Ti-Zr-Y discrimination diagram of *Pearce and Cann* [1973]. Many other tectonic discrimination diagrams illustrate that the Attunga eclogite protolith is likely to be ocean crust formed proximal to a convergent plate boundary (Figure 5). Plotted on a primitive mantle normalized spider diagram (Figure 4), ATE02 is slightly more enriched in LREE relative to ATE01. Apart from this minor difference, they both have similar signatures and indicate a depleted harzburgitic mantle source which is a consistent signature throughout most of the Weraerai terrane [*Rogers*, 1986; *Breyley*, 1990; *Aitchison et al*., 1994; *Yang and Seccombe*, 1997]. *Yang and Seccombe* [1997] also suggested that dolerites contained within the serpentinite mélange along this northern portion of the Weraerai terrane near Attunga are transitional in nature between MORB and island arc basalts. This is due to their flat to very slight LREE enrichment relative to the HREE and minor depletion of Ti, which are indicative of a suprasubduction zone ophiolite setting. Large anomalies of Ba and U are thought to be the product of metamorphism/metasomatism. Thus, a suprasubduction zone setting is proposed for the formation of the Attunga eclogite gabbro protolith.

Two previous zircon studies have been carried out on the Attunga eclogite to constrain the protolith and timing of metamorphism. The first was an abstract by *Watanabe et al*. [1999], who provided an undocumented magmatic zircon age of 650 Ma and an eclogite metamorphic zircon age of 570 Ma. More recently, *Phillips et al*. [2015] reported U-Pb zircon ages to 520 Ma and 480 Ma. They suggest that both of these ages represent eclogite facies metamorphism, based on the depleted HREE content of zircons analyzed and therefore coeval growth with garnet. This interpretation requires the age for the protolith to be older than the Early Cambrian metamorphic age with this protolith age unknown. Our results confirm that two distinct U-Pb zircon ages occur, both of which are within error for those proposed by *Phillips et al*. [2015]. However, in contrast to the conclusion reached by *Phillips et al*. [2015], we do make clear distinctions between the dark CL cores, corresponding to an older igneous age of ~530 Ma and the lighter patchy zircon, corresponding to a younger U-Pb age of ~490 Ma. *Phillips et al*. [2015] describe one zircon with an older rim age than the core of the same zircon (473 ± 8 Ma and 507 ± 8 Ma, respectively). The authors use this relationship in a single zircon to argue for two separate periods of metamorphism. We suggest that this is a reflection of the complexity associated with the interpretation of U-Pb isotopic systems in recrystallized and/or zircon affected by metamorphism, whereby high-U zircon can lose more radiogenic Pb in later events. Generally, our zircon rims and recrystallized zones fell into the younger ~490 Ma age, while igneous cores were ~520 Ma.

Our argument that these zircon cores represent earlier magmatic crystallization event is reinforced by our zircon REE data. REE patterns for type I zircon are typical of magmatic zircons that have grown in the presence of plagioclase crystals which have preferentially scavenged Eu^{2+} (substituting for Ca^{2+}) [*Weill*, 1973]. Type I

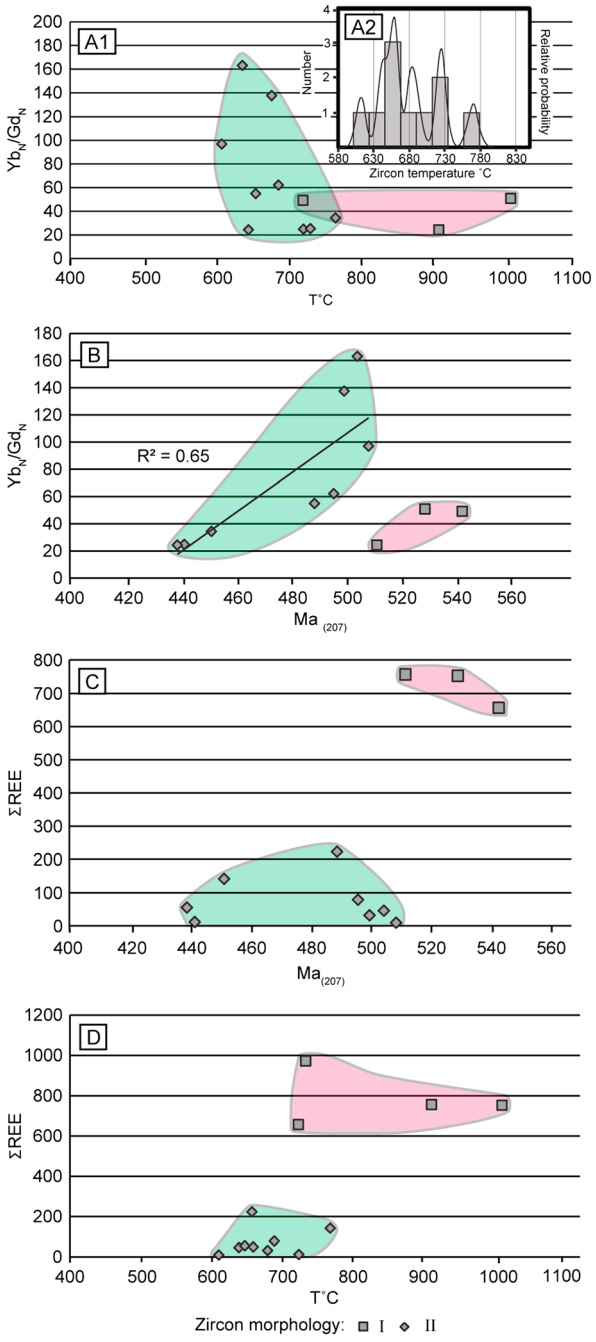

Figure 13. Zircon REE, U-Pb, and Ti-in-zircon comparisons. A1: Yb_N/Gd_N versus Ti-in-zircon calculation temperature for individual zircon. Diamonds with green overlay are type II zircon; squares with pink overlay are type I zircon. There is no noticeable correlation between an increase in the temperature based on the Yb_N/Gd_N ratio. A2: Temperature histogram from type II zircon, based on Ti-in-zircon thermometry method of *Watson et al.* [2006], where by zircon formation if in equilibrium with rutile and quartz. Average temperature for the type II zircon is ~685°C. (b) Yb_N/Gd_N versus 207 corrected U-Pb zircon age. A trend line is plotted for type II zircon only. A weak positive correlation is seen between Yb_N/Gd_N versus 207 corrected U-Pb zircon age, R^2 = 0.65. Higher Yb_N/Gd_N values correspond to an enrichment in HREE. (c) Total REE ppm (ΣREE) versus 207 corrected U-Pb zircon ages. (d) A clear distinction between type I and type II zircons is seen based on their ΣREE values.

zircons also exhibit positive Ce anomalies in comparison to type II. Magmatic zircons are often characterized by this feature due to the propensity of Ce(IV) to be incorporated into zircon during crystallization [*Ballard et al.*, 2002].

In addition to U-Pb and REE zircon data, we provide Lu-Hf data on the zircons to constrain the relative influence that continental crust may have had during crystallization and hence establish if the protolith was essentially juvenile oceanic crust or a continental affected marginal ocean. The Lu-Hf isotopic system within zircon is often described as being robust, even if there has been a disturbance to the zircon crystal lattice which hosts it [*Hoskin and Black*, 2000]. Zircons crystallized from either fluids or a secondary melt, under metamorphic conditions, exhibit initial $^{176}Lu/^{177}Hf$ ratios mirroring the rock matrix. These ratios are usually greater than 0.014 [*Gerdes and Zeh*, 2009]. When compared to igneous zircon, which retain higher portions of nonradiogenic Hf, lower initial $^{176}Lu/^{177}Hf$ are observed ($<$0.002). For the Attunga zircons, we see very similar $^{176}Lu/^{177}Hf$ ratios for both type 1 and type II zircons, of which the ratio is near equivalent to zircons from an igneous source ($<$0.002) [*Gerdes and Zeh*, 2009].

The U-Pb age of ~530 Ma for Attunga type I zircon is within error of the average Hf $T_{(DM)}$ model age of ~550 Ma. This indicates that the magmatic protolith was derived entirely from a juvenile depleted mantle source, with no detectable input from an older crustal reservoir [*Griffin et al.*, 2004]. Thus, if the protolith of the Attunga eclogite were associated with back-arc spreading behind a long-lived Andean-type arc on the Gondwanan margin, or it was influenced by the subduction of sediments derived from continental areas, zircons would be expected to show a spread toward lower initial

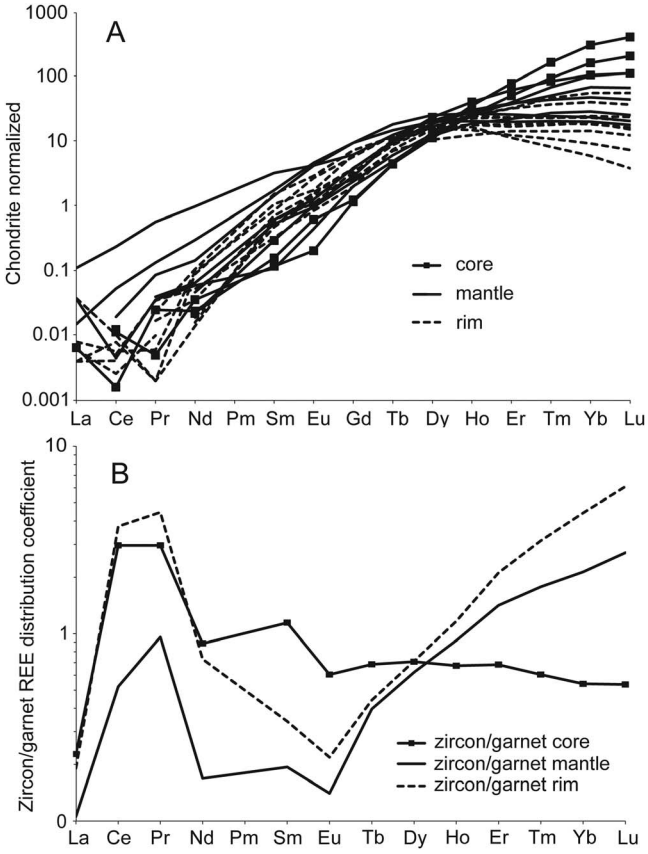

Figure 14. (a) Chondrite normalized REE values for separate garnet domain. (b) REE partition coefficients between zircon and coexisting garnet. Calculated from the average elemental content for each domain (core, mantle, and rim).

$\varepsilon Hf_{(t)}$. An example of continental affected ocean crust is the Paleozoic Moeche Ophiolite, NW Iberia [*Arenas et al*., 2014], and the Cuomuqu ophiolite in North Tibet [*Zhengxin et al*., 2015]. The Moeche Ophiolite is sourced from a short-lived ocean basin formed in a proximal continental setting in the Devonian. Initial $\varepsilon Hf_{(t)}$ values of less than −5 for Devonian zircon illustrate that their source was not juvenile in nature and hence were not formed in the Rheic Ocean distal from continental crust [*Arenas et al*., 2014]. Furthermore, the presence of Proterozoic xenocrysts in the Moeche Ophiolite is direct evidence of the involvement of older crust. The Meso-Tethys Middle-Late Jurassic Cuomuqu ophiolite has initial $\varepsilon Hf_{(t)}$ values of −16.1 to +10.1, with most being between +2.8 and +7.6. The Cuomuqu ophiolite is interpreted to have formed in a back arc, behind an intra-oceanic (boninitic) island arc. Rare negative $\varepsilon Hf_{(t)}$ values may originate from the subduction of minor amounts of continental sediment [*Zhengxin et al*., 2015]. The setting proposed for the formation of the Attunga eclogite by *Phillips et al*. [2015] is similar to the Paleozoic Moeche and Jurassic Cuomuqu ophiolites in regard to its proximity to continental crust. However, this interpretation is incompatible with our highly positive Hf isotopic data.

The $\varepsilon Hf_{(t)}$ values of ~14 clearly demonstrate a juvenile depleted mantle source for the Attunga eclogite protolith (Figure 15), with no continental influence. So either the ophiolitic protolith developed within a nascent intra-oceanic island arc or it developed in a back arc or setting that was so extensive as to remove any influence of continental crust. The Tonga-Kermadec arc [*Kemp et al*., 2009] may be a valid modern analogue of the back-arc model where spreading in the Tasman Sea removed slivers of the Australian crust to New Zealand and the Lord Howe rise [*Cluzel et al*., 2001] before the arc developed in an entirely intra-oceanic setting. However, there is no geological evidence of older Delamerian continental crustal ribbons or Gondwanan inheritance within the early Paleozoic (pre-latest Devonian) rocks of the New England Orogen. All that can be said is that the juvenile ~530–520 Ma oceanic crust the protolith of the Attunga eclogite was subducted and eclogitized by ~490 Ma. We suggest that the simplest and most likely tectonic setting for this to occur is within a fore-arc region where a suprasubduction zone ophiolitic basement is tectonically eroded by the downgoing plate and subsequently eclogitized with the cycle of fore-arc ophiolite formation to consumption taking 30–40 Ma in this case.

7.2. Eclogite Metamorphism

In the Attunga zircon we see two discrete events, ~530 Ma and ~490 Ma. Low Th/U ratios <0.1 found in ATE01 type II zircons are characteristic for metamorphic/recrystallized zircon [*Hoskin and Black*, 2000; *Rubatto*, 2002; *Corfu et al*., 2003], along with homogeneous or sector-zoned structures in CL images. The decrease in the U, Th contents from >150 ppm for magmatic cores and <10 ppm for metamorphic zircon

Table 6. Garnet REE Contents From ATE01

Domain	Core	Rim	Mantle	Rim	Mantle	Rim	Mantle	Rim	Core	Rim	Mantle	Rim	Mantle	Rim	Core	Rim	Mantle	Rim
Garnet	1		2		3		4		5		6		7		8		9	
Spot	1-1C	1-1R	1–2C	1–2R	1–3C	1–3R	1–4C	1–4R	1–5C	1–5R	1-6C	1-6R	1-7C	1-7R	1–8C	1–8R	1–9C	1–9R
La	0.01	0.01	0.01	0.01	0.01	0.01	0.01	0.01	0.01	0.01	0.01	0.01	0.01	0.01	0.01	0.01	0.04	0.01
Ce	0.01	0.01	0.05	0.01	0.02	0.01	0.01	0.01	0.01	0.01	0.01	0.00	0.01	0.01	0.01	0.01	0.23	0.01
Pr	0.01	0.00	0.02	0.01	0.01	0.00	0.00	0.01	0.01	0.00	0.01	0.01	0.01	0.00	0.01	0.00	0.08	0.00
Nd	0.04	0.03	0.22	0.08	0.10	0.04	0.04	0.03	0.03	0.03	0.03	0.03	0.05	0.06	0.04	0.07	0.71	0.04
Sm	0.07	0.17	0.41	0.36	0.34	0.11	0.04	0.11	0.03	0.14	0.12	0.15	0.15	0.25	0.06	0.20	0.76	0.08
Eu	0.09	0.14	0.41	0.26	0.37	0.14	0.04	0.11	0.02	0.13	0.09	0.10	0.11	0.16	0.05	0.24	0.38	0.08
Gd	0.91	1.16	2.97	2.28	2.97	1.19	0.63	1.21	0.36	0.82	0.75	1.05	1.20	1.92	0.38	1.81	1.94	0.62
Tb	0.61	0.62	0.88	0.70	1.09	0.60	0.29	0.56	0.26	0.42	0.36	0.52	0.59	0.73	0.27	0.73	0.74	0.44
Dy	9.19	6.64	7.88	6.20	9.97	6.12	4.76	6.68	5.38	4.13	5.03	6.60	7.33	7.82	4.41	6.27	8.19	6.01
Ho	3.55	1.45	1.79	1.30	2.34	1.60	1.66	1.97	3.12	1.09	2.14	2.23	2.52	2.18	2.27	1.57	2.67	2.16
Er	15.83	2.91	5.10	3.17	6.63	4.64	5.70	6.04	20.04	3.66	10.21	8.38	9.64	5.94	12.95	4.32	9.88	8.28
Tm	3.09	0.30	0.75	0.40	0.90	0.69	1.00	0.84	6.10	0.52	2.49	1.70	1.86	0.85	3.46	0.66	1.62	1.36
Yb	27.00	1.51	5.12	2.34	6.01	4.70	7.37	6.25	78.39	3.68	26.13	14.25	17.50	5.92	41.50	4.93	12.15	10.32
Lu	4.42	0.15	0.71	0.29	0.81	0.64	1.00	0.93	16.00	0.48	4.42	2.18	2.62	0.81	8.13	0.60	1.74	1.45
Eu/Eu[a]	1.09	0.94	1.14	0.87	1.13	1.21	0.95	0.93	0.55	1.15	0.85	0.76	0.82	0.68	1.40	1.22	0.94	1.05
Lu_N/Dy_N[b]	4.81	0.23	0.89	0.46	0.81	1.04	2.09	1.39	29.74	1.17	8.77	3.31	3.57	1.03	18.45	0.96	2.13	2.42
Core/rim (Lu_N/Dy_N)[b]	21.36		1.94		0.78		1.50		25.38		2.65		3.47		19.32		0.88	

[a] $Eu = \sqrt{(Sm_N \times Gd_N)}$.
[b] N = element normalized to chondrite.

has been noted for eclogite facies zircon from other terranes [*Gebauer et al*., 1997; *Liati and Gebauer*, 1999; *Rubatto et al*., 1999; *Zheng et al*., 2005]. Thus, we agree with *Phillips et al*. [2015] that high-grade (eclogite) facies metamorphism occurred at 490–480 Ma, but our REE data indicate that the ~530 Ma cores are igneous zircons equivalent to the ~530 Ma gabbros at Bingara hosted in the same serpentinite mélange (Weraerai terrane).

Based on REE contents, three types of garnet morphology exist, core, mantle, and rim. Garnet cores are characterized by HREE enrichment with a subsequent steep REE profile and negligible Eu anomalies. This type is restricted to inclusion-rich cores of larger garnets (>500 μm). No analysis was taken between these cores and their rims, though smaller, inclusion-free garnet cores are represented by intermediate HREE contents between core and rim values with the latter having flat to depressed HREE contents. No Eu anomalies are seen in any of the garnet domains, suggesting that plagioclase was not stable during the formation of garnet.

Table 7. Trace Element Partition Coefficients Between Zircon and Garnet

	Gt. Core[a]	Gt. Mantle	Gt. Rim
La	0.23	0.11	0.19
Ce	2.96	0.52	3.74
Pr	2.96	0.96	4.45
Nd	0.89	0.17	0.73
Sm	1.14	0.19	0.34
Eu	0.61	0.14	0.22
Tb	0.69	0.40	0.44
Dy	0.71	0.62	0.71
Ho	0.67	0.92	1.16
Er	0.68	1.42	2.11
Tm	0.61	1.78	3.14
Yb	0.54	2.14	4.41
Lu	0.54	2.71	6.09
Hf	45,825	2,462	110,162
Lu/Dy[b]	0.76	4.35	8.53

[a] Calculated from average core, mantle, and rim composition.
[b] Ratio of coefficient values.

Depletion of HREE from core > mantle > rim is reinforced by $REE_{Dzr/grt}$ trace element partition coefficients (Figure 14b). Early garnet cores formed in the absence of recrystallizing zircon at high enough metamorphic pressure for plagioclase not to be stable. This is based on the $(La/Dy)_{Dzr/grt\ core}$ values which are close to 1.0. Mantle $(La/Dy)_{Dzr/grt\ mantle}$ garnet values are ~4.4 and garnet rim values are ~8.5. This indicated that intermediate garnet mantle growth was crystallizing in an environment where zircon was starting to compete with garnet for HREE, with rim values showing the most extreme values. These REE trace element partition coefficient

AGU Tectonics

10.1002/2016TC004408

Table 8. Summary of Zircon LA-ICP-MS Lu-Hf Data[a]

Sample	$^{174}Hf/^{177}Hf$	1SE	$^{178}Hf/^{177}Hf$	1SE	$^{176}Lu/^{177}Hf$	1SE	$^{176}Hf/^{177}Hf$	1SE	$\varepsilon Hf(0)$[a]	U/Pb Age (Ma)	Initial $^{176}Hf/^{177}Hf$	$\varepsilon Hf(t)$[b]	$T_{(DM)}$(Ga)[c]
AT-2.1	0.008672	0.000008	1.467694	0.000039	0.000060	0.000002	0.282912	0.000012	4.50 ± 0.43	505	0.28291	15.7 ± 0.7	0.46
AT-2.2	0.008658	0.000013	1.467728	0.000056	0.000131	0.000001	0.282909	0.000015	4.39 ± 0.55	496	0.28291	15.4 ± 0.7	0.47
AT-2.3	0.008658	0.000007	1.467734	0.000083	0.000046	0.000000	0.282921	0.000026	4.81 ± 0.93	477	0.28292	15.4 ± 1.1	0.45
AT-4.1	0.008658	0.000015	1.467603	0.000072	0.000134	0.000011	0.282848	0.000015	2.24 ± 0.55	452	0.28285	12.3 ± 0.7	0.55
AT-4.1	0.008655	0.000017	1.467590	0.000080	0.000146	0.000010	0.282863	0.000016	2.76 ± 0.58	452	0.28286	12.8 ± 0.8	0.53
AT-5.2	0.008672	0.000010	1.467735	0.000047	0.000031	0.000000	0.282904	0.000011	4.20 ± 0.40	442	0.28290	14.0 ± 0.6	0.48
AT-6.1	0.008674	0.000010	1.467684	0.000042	0.000074	0.000003	0.282836	0.000012	1.79 ± 0.43	515	0.28284	13.3 ± 0.7	0.57
AT-6.2	0.008649	0.000013	1.467677	0.000057	0.000604	0.000011	0.282798	0.000015	0.48 ± 0.53	515	0.28279	11.7 ± 0.7	0.63
AT-7.1	0.008666	0.000012	1.467622	0.000069	0.000034	0.000001	0.282808	0.000018	0.80 ± 0.63	472	0.28281	11.3 ± 0.8	0.61
AT-8.1	0.008674	0.000008	1.467737	0.000044	0.000365	0.000010	0.282909	0.000011	4.39 ± 0.38	489	0.28291	15.2 ± 0.6	0.47
AT-8.2	0.008681	0.000010	1.467744	0.000054	0.000099	0.000003	0.282888	0.000011	3.65 ± 0.39	489	0.28289	14.5 ± 0.6	0.50
AT-9.1	0.008750	0.000029	1.467834	0.000057	0.002638	0.000058	0.282996	0.000020	7.45 ± 0.72	543	0.28297	18.6 ± 0.9	0.37
AT-10.1	0.008564	0.000031	1.467669	0.000034	0.001981	0.000109	0.282836	0.000017	1.79 ± 0.61	533	0.28282	13.0 ± 0.8	0.60
AT-10.2	0.008616	0.000027	1.467662	0.000054	0.001736	0.000076	0.282828	0.000015	1.53 ± 0.52	533	0.28281	12.8 ± 0.7	0.61
AT-11.1	0.008678	0.000010	1.467742	0.000047	0.000119	0.000006	0.282875	0.000011	3.20 ± 0.41	473	0.28287	13.7 ± 0.6	0.52
AT-12.1	0.008671	0.000015	1.467820	0.000058	0.001697	0.000029	0.282951	0.000016	5.89 ± 0.55	500	0.28294	16.5 ± 0.7	0.43
AT-13.1	0.008578	0.000034	1.467524	0.000102	0.001567	0.000054	0.282617	0.000045	−5.95 ± 1.59	528	0.28260	5.3 ± 1.7	0.90
AT-14.1	0.008669	0.000008	1.467604	0.000040	0.000485	0.000005	0.282741	0.000012	−1.55 ± 0.44	530	0.28274	10.1 ± 0.7	0.71
AT-15.1	0.008625	0.000009	1.467668	0.000056	0.000734	0.000053	0.282817	0.000013	1.13 ± 0.46	498	0.28281	12.0 ± 0.7	0.61
AT-16.1	0.008672	0.000008	1.467649	0.000046	0.000030	0.000000	0.282839	0.000015	1.90 ± 0.52	439	0.28284	11.7 ± 0.7	0.56
AT-17.1	0.008672	0.000012	1.467643	0.000039	0.001165	0.000003	0.282811	0.000010	0.91 ± 0.35	512	0.28280	11.9 ± 0.6	0.62
AT-18.1	0.008667	0.000007	1.467658	0.000040	0.000134	0.000001	0.282902	0.000013	4.13 ± 0.45	589	0.28290	17.2 ± 0.7	0.48
AT-19.1[d]	0.008660	0.000010	1.467740	0.000040	0.000869	0.000005	0.282836	0.000010	1.79 ± 0.36	503	0.28283	12.7 ± 0.6	0.58
AT-20.1[d]	0.008659	0.000018	1.467612	0.000057	0.002906	0.000010	0.282818	0.000019	1.16 ± 0.67	503	0.28279	11.4 ± 0.8	0.64
AT-21.1[d]	0.008637	0.000011	1.467647	0.000044	0.001407	0.000021	0.282853	0.000013	2.40 ± 0.45	503	0.28284	13.1 ± 0.7	0.57
AT-22.1[d]	0.008622	0.000014	1.467621	0.000048	0.003080	0.000019	0.282784	0.000012	−0.04 ± 0.42	503	0.28275	10.1 ± 0.7	0.69
AT-23.1[d]	0.008646	0.000021	1.467754	0.000043	0.002486	0.000026	0.282865	0.000013	2.81 ± 0.45	503	0.28284	13.2 ± 0.7	0.56

[a]CHUR values from *Bouvier et al*. [2008].
[b]This uncertainty is the combined in-run standard error and the external reproducibility of standards for each session added in quadrature.
[c]Depleted mantle model ages calculated using estimates of $^{176}Hf/^{177}Hf = 0.283251$ and $^{176}Lu/^{177}Hf = 0.0389$ for the modern upper mantle. N.D. no SHRIMP U-Pb analyses available for these grains.
[d]Lu-Hf analysis undertaken on sites without U-Pb age. Average U-Pb zircon age used to determine initial isotopic values and $T_{(DM)}$ model ages.

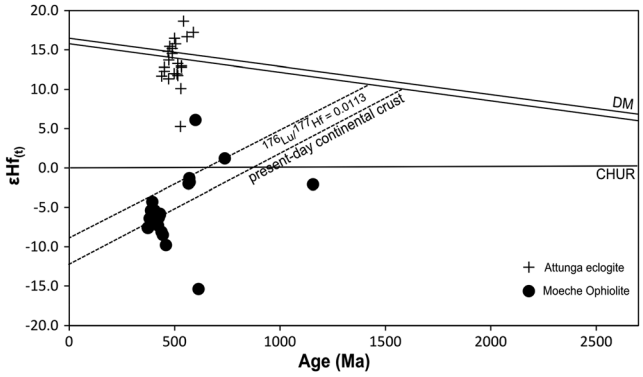

Figure 15. $\varepsilon Hf_{(t)}$ values versus U-Pb zircon ages. $\varepsilon Hf_{(t)}$ values for the Attunga zircons lie on the DM-MORB line. $\varepsilon Hf_{(t)}$ values from the Moeche Ophiolite, NW Iberia [*Arenas et al*., 2014], have been added to illustrate the formation of mafic crust in a continental rift setting whereby juvenile magmas have interacted with older continental crust. DM (depleted mantle) values from *Nowell et al*. [1998]. Present-day continental crust $^{176}Lu/^{177}Hf$ ratios of 0.0113 from *Wedepohl* [1995].

values are comparable to data presented by *Rubatto* [2002] with the author presenting $(La/Dy)_{Dzr/grt\ core} = 0.5$ and $(La/Dy)_{Dzr/grt\ rim} = 3.0$. Similar results are also presented by *Schaltegger et al*. [1999] and *Rubatto and Hermann* [2003].

The determination of the pressure and temperature conditions for the Attunga eclogite by *Shaw and Flood* [1974] relied on the partitioning of Fe and Mg between coexisting garnet and pyroxene. Their results derived temperatures in the range 290–600°C at 7–12 Kb. Issues associated Fe and Mg ion exchange include the assumption that the cores of garnet and omphacite are at equilibrium with one another at peak metamorphic conditions [*Krogh Ravna and Paquin*, 2003]. This method also relies heavily on the oxidation state of iron in garnet and pyroxene. This is often unknown, or calculated with a large margin of error [*Spear*, 1993; *Carswell and Zhang*, 1999], with some authors suggesting that the associated error may be as large as ±85°C [*Krogh Ravna and Terry*, 2004] to ±100°C [*Carswell and Zhang*, 1999].

An alternative thermometer is offered by the distribution of Ti-in-zircon, found in equilibrium with rutile in quartz. *Watson and Harrison* [2005] propose that the Ti-in-zircon thermometer usually incurs errors of ±10°C or less, and thus, this is more robust than garnet-pyroxene cation exchange thermometer. A requirement for accurate thermometry by Ti-in-zircon method is that zircon is in equilibrium with quartz and rutile. Figures 6a1 and 6a2 illustrates rutile forming prior to regressive titanite rims. Recrystallized type II zircon domains are in equilibrium with these rutile cores. Rutile and quartz are preserved as inclusions within omphacite (Figures 6f and 6g). The Ti-in-zircon temperatures for Attunga metamorphic zircon range from 612 to 770°C. This ~160°C range of zircon metamorphic zircon growth in eclogite facies rocks has also been described by *Di Vinchenzo et al*. [1997], *Zheng et al*. [2005], and *Ota and Kaneko* [2010].

Mineral inclusions within the cores of large garnets include quartz, albite, and epidote (Figure S2 and Table S2). With the exception of quartz, none of these minerals are stable at peak eclogite metamorphic conditions [*Holland*, 1983]. Garnet possibly acts as a pressure vessel, shielding lower grade metamorphic mineral phases as reported elsewhere [*Di Vincenzo et al*., 2016]. *Phillips et al*. [2015] propose that the cores of the larger garnets represent peak conditions, due to the presence of glaucophane, lawsonite, and high-pressure omphacite. They used these mineral phases to calculate peak metamorphic conditions. We did not find these mineral phases in our investigations, and therefore, our P/T history may differ slightly from that of *Phillips et al*. [2015]. Peak metamorphic conditions were slightly higher based on our Ti-in-zircon data (blue area, Figure 16). The retrograde path passed between the rutile/titanite and garnet stability field (green area, Figure 16). Here the jadeite content (Jd = ~20) of the matrix omphacite is reached. All of these occur at a slightly higher pressure than that proposed by *Phillips et al*. [2015].

We propose that type II zircon occurred around peak metamorphic conditions (<770°C). Scant data from Figure 13b may demonstrate that apparently younger type II zircon has lower HREE contents, whereas apparently older ones have higher HREE contents, which may reflect zircon's preference to host HREE over garnet [*Rubatto*, 2002]. This could demonstrate a prograde environment for the type II zircons displaying apparent lower temperatures. Thin zircon rims (type III) are present around many of type I and II zircons (Figure 9). In most cases they are too thin for SHRIMP or LA-ICP-MS analysis and therefore our interpretation of them is limited. These thin zircon rims are, however, common in terranes which have undergone metamorphism while in the presence of high fluid flux, which allows the relative immobile zircon to undergo dissolution and reprecipitation [*Wayne and Sinha*, 1992; *Williams et al*., 1996; *Hacker et al*., 1998].

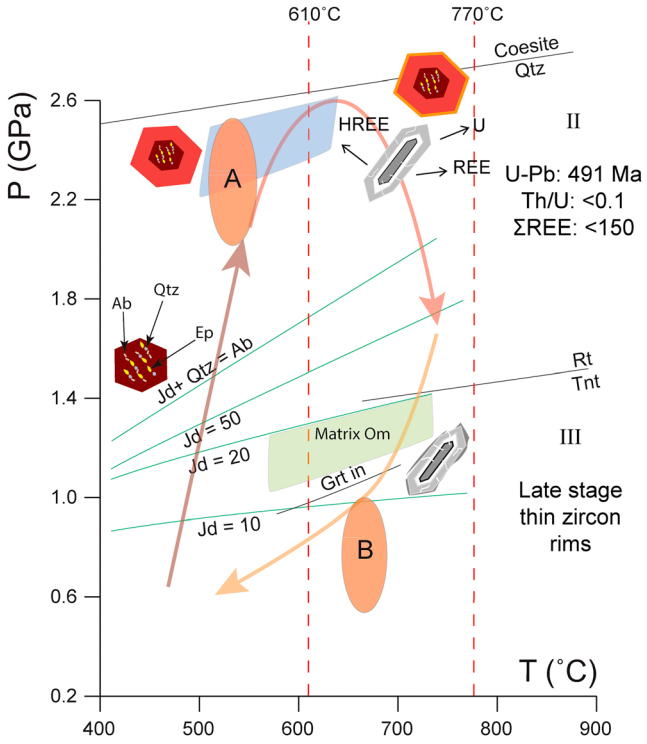

Figure 16. P-T path for the Attunga eclogite combined with data from *Phillips et al.* [2015]. Initial garnet growth, with the inclusion of albite (Ab), quartz (Qtz), and epidote (Ep). Peak pressure reached at 2.2 GPa [after *Phillips et al.*, 2015]. Increase of temperature with the eclogite moving out of the epidote stability field, while garnet growth continued. Ti-in-zircon thermometry indicates that zircon recrystallization occurred between 610 and 770°. This was coeval with garnet growth. Matrix pyroxene equilibrated at a lower temperature with an average jadeite composition of 20 (Jd = 20) from the analysis in this study. This is in agreement with *Phillips et al.* [2015]. Peak temperature calculation by *Phillips et al.* [2015] place this position at a lower pressure, though the P-T trajectory plotted here still passes through it. (a) Peak pressure calculated from $garnet_{core}$-omphicate thermometry from *Phillips et al.* [2015]. (b) Peak temperature from $garnet_{rim}$-matrix omphacite and jadeite barometry calculations from *Phillips et al.* [2015]. Jadeite isopleths after *Holland* [1983]. Garnet curve after *Poli* [1993] Rutile (Rt) and titanite (Tnt).

7.3. Eclogite Emplacement and Tectonic Evolution

$^{40}Ar/^{39}Ar$ ages for blueschist-lawsonite blocks from Glenrock and Pigna Barney, by *Phillips et al.* [2015], are within error with eclogite facies metamorphism for the Attunga eclogite presented here. Previously, Middle Ordovician K-Ar ages (465–480 Ma) [*Fukui et al.*, 1995] for these samples have always been treated with caution, due to difficulties arising from excess argon giving erroneous older ages [*Kelley*, 2002]. Age data presented by *Phillips et al.* [2015] on these blueschist blocks may suggest two things: (1) these mafic blocks were exposed to blueschist-eclogite facies conditions within the same subduction zone which was responsible for the Attunga eclogite at 480–490 Ma or (2) there has been an amalgamation of two separate metamorphic terranes, such as shown for the Motagua fault zone, Guatemala [*Harlow et al.*, 2004]. We favor the simpler first interpretation.

The mechanisms which lead to the detachment and exhumation of dense HP-LT metamorphic rocks within convergent margins are still poorly understood [*Ring et al.*, 1999; *Jolivet et al.*, 2003; *Agard et al.*, 2009]. Numerous models have been proposed in order to explain decoupling of these rocks from the downgoing plate. These have been outlined by *Guillot et al.* [2009], and they include corner flow [*Platt*, 1986], channel flow [*Cloos*, 1982], extensional collapse [*Dewey et al.*, 1993], buoyancy assisted by erosion and tectonic processes [*Chemenda et al.*, 1995], and formation of a serpentinite channel [*Guillot et al.*, 2001]. Out of these processes, only the latter two are thought to be responsible for the movement of allochthonous HP-LT blocks from depths no greater than 70 km [*Burov et al.*, 2001; *Agard et al.*, 2009] back to the surface in a serpentinite mélange. It has been found that the exhumation of these HP-LT oceanic materials is not a continual process and across most paleoconvergent margins are constrained to discrete 10–50 Ma time periods [*Agard et al.*, 2009]. Examples of perturbations include initiation of subduction [*Anczkiewicz et al.*, 2004], subduction of buoyant material [*Ernst*, 1988; *Cloos*, 1993; *Arculus et al.*, 1999; *Ernst*, 2001], change in convergence direction [*Agard et al.*, 2006], and slab break off [*Von Blanckenburg and Huw Davies*, 1995]. These can occur at any point during convergence, and therefore, changes to the "normal" state of convergence are needed in order to exhume metamorphosed unites to the surface.

Due to the Attunga eclogite's intimate relationship with its serpentinite mélange host, we also suggest that initial removal from either the downgoing slab (footwall) or the hanging wall of the overriding plate was via an active serpentinite channel and low-density serpentinite diapirs rising from it. Serpentinite may have been sourced either from peridotite of the subducted oceanic crust [*Chalot-Prat et al.*, 2003; *Whitney and Davis*,

2006] or from the hydration of the mantle wedge [*Guillot et al*., 2001; *Scambelluri et al*., 2001; *Fitzherbert et al*., 2004; *Guillot et al*., 2004]. A modern analog for this may be the setting, giving rise to the serpentinite/mud volcanoes in the fore-arc region of the Izu-Bonin-Mariana arc that extrude blueschist blocks [*Fryer et al*., 1999].

The model proposed by *Phillips et al*. [2015] for the exhumation of the Attunga eclogite revolves around the forced flow of high-pressure rocks upward, with their preservation located below the evolving arc edifice. Even after extensive rollback extension, the high-pressure assemblages and the ophiolite would have been coupled to the convergent margin. Hence, formation of the Attunga eclogite in this model occurred during an incipient period of low-angle subduction in the Cambrian. Following this, Phillips et al. suggest that the eclogite was preserved beneath its suprasubduction zone protolith, which itself was located below the continental basement of eastern Gondwana, as part of the Delamerian Orogen until its exhumation to the surface in the Early Permian. Only a few eclogites worldwide have been specifically associated with slab rollback and exhumation, and these include eclogites in the Mediterranean [*Jolivet et al*., 2003]. Typically, these eclogites are associated with asthenospheric upwelling and characterized by garnet peridotites [*Medaris*, 1999]. However, garnet peridotites are yet to be discovered anywhere in the Tasmanides.

While the analysis of a single eclogite cannot determine subduction polarity, the geological context of the host and neighboring rocks can provide ample evidence. The long-lived westerly dipping subduction models [*Leitch*, 1975; *Cawood*, 1983; *Phillips et al*., 2015] would have the Attunga eclogite forming in the same subduction zone responsible for the Delamerian Orogen during the Late Cambrian before being rifted and being incorporated into the New England Orogen as a ribbon of older continental crust separate from Gondwana by an extensive back-arc basin.

Phillips et al. [2015] suggest that the Attunga eclogite formed in a fore-arc marginal to Gondwana between 540 and 530 Ma and may be spatially connected to the Delamerian Orogeny. In their model, high-pressure rocks were preserved in the fore arc of the Macquarie Arc, above a westerly dipping slab, where they remained at 30–53 km depth with their HP assemblages surviving despite numerous later orogenic events and extensive plutonism, until their exhumation to the surface at 280 Ma [*Lanphere and Hockley*, 1976; *Shaw and Flood*, 1981; *Korsch and Harrington*, 1987; *Offler and Foster*, 2008; *Shaanan et al*., 2015]. This model does not accommodate any addition of exotic Panthalassa oceanic crustal material via a more complex subduction architecture throughout the entire ~300 Ma evolution of the Tasmanides. The model suggests that the tectonic evolution of eastern Gondwana was somehow uniquely devoid of arc-continent collisions despite the numerous examples of arc-continent collisions in modern and ancient orogens, for example, Taiwan [*Huang et al*., 2008], Oman [*Searle et al*., 2004], the ancient southern margin of Tethys in Ladakh [*Corfield et al*., 1999], Cyprus [*Robertson*, 2004], and the Kamchatka Peninsula in the NW Pacific [*Hourigan et al*., 2009].

We feel that there is insufficient data to make comparisons to existing tectonostratigraphic elements within the Delamerian Orogen some 1200 km to the west, even though the Delamerian ophiolites are of similar age to the Attunga eclogite. Instead, we do point out that the Attunga eclogite protolith age is identical, within error, of the nearby ophiolitic plagiogranites and gabbros dated by *Aitchison and Ireland* [1995] within the serpentinite mélange along strike at Bingara only 100 km away. It is likely that terranes associated with the Cambrian Attunga eclogite interacted with other intra-oceanic terranes (i.e., the Gamilaroi island arc terrane) prior to its accretion in the Devonian [*Stratford and Aitchison*, 1997] and that these interactions may have been the precursor for the initial exhumation of the Attunga eclogite, along the Peel Fault during the Early Permian.

We favor building on the alternative model of island arc collision associated with a period of east dipping subduction before collision and a subduction flip, as was originally proposed by *Aitchison and Flood* [1994] and later supported by *Offler and Murray* [2011] and *Glen* [2013] (Figure 2). We suggest that the Attunga rocks must have been exhumed to high crustal levels shortly after they experienced peak P-T in order to avoid complete retrogression (Figure 17). The eclogite blocks were preserved in a separate Panthalassa intra-oceanic subduction system not associated with the Macquarie Arc or Delamerian Orogen (Figure 2). Modification of the serpentinite to its present form along the Peel Fault most likely did not occur until the Early Permian, based on the earliest occurrence of serpentinite clasts in the Early Permian Manning Group [*Offler and Williams*, 1987; *Aitchison and Flood*, 1992; *Aitchison et al*., 1997] and their absence in older sedimentary sequences in the region.

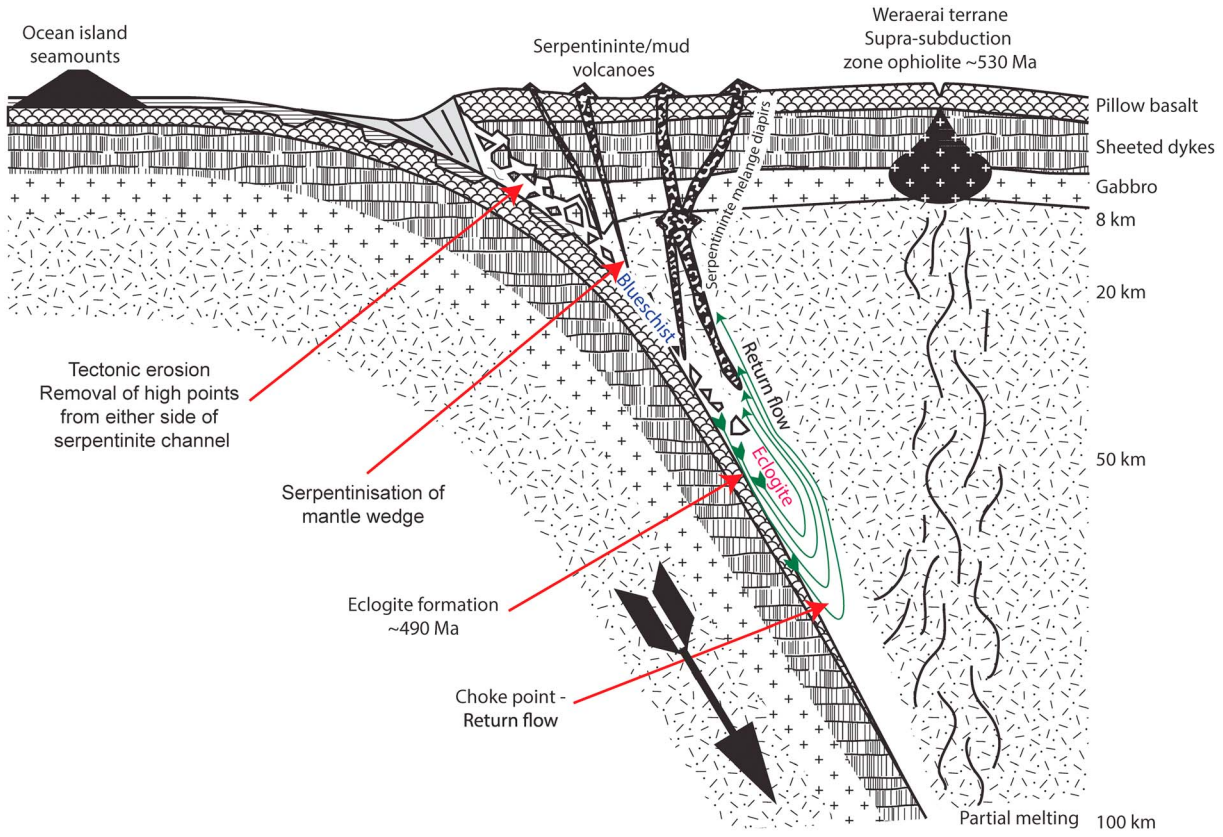

Figure 17. Upward migration of serpentinite below a nascent oceanic island arc results in the mixing of material of differing metamorphic grade and age. Surface expression may resemble the modern serpentinite mud volcanoes of the Izu-Bonin-Mariana fore arc. Rocks from either side of the serpentinite channel are plucked off and incorporated into the mélange.

Other occurrences of Cambro-Ordovician units along the Peel Fault are rare, and their relationship to one another is difficult to establish. These early Paleozoic units include volcanoclastic rocks of the Murrawong Formation [*Stewart*, 1995; *Furey-Greig*, 1999, 2000], Early to Middle Ordovician blueschist blocks at Pigna Barney and Glenrock [*Fukui et al*., 1995; *Och et al*., 2003], and a 445 Ma U-Pb zircon age for an amphibolized gabbro block [*Offler and Shaw*, 2006]. It is likely that these early Paleozoic units developed in a similar or the same intra-oceanic subduction system as the Attunga eclogite but importantly they contain no Gondwana inheritance.

Other Paleozoic Panthalassa Ocean-derived exotic terranes have been identified elsewhere around the circum-Pacific as having been accreted onto active continental margins. These include the Late Silurian to Late Devonian Pearya and Alaska-Chukota terranes which accreted onto the northern Laurentia margin [*Hadlari et al*., 2013; *Nekrasov and Bogomolov*, 2015] and the Carboniferous to Permian Chilenia and Patagonia terranes accreted onto the west Gondwanide margin [*Willner et al*., 2010; *Martínez et al*., 2012]. Both of these margins are not dissimilar to the Tasmanides and the New England Orogen, with a combination of continental margin subduction and allochthonous terrane accretion contributing to the creation of continental crust.

Our zircon morphology, geochronology, zircon/garnet REE, and Hf isotope data indicate that the protolith for the Attunga eclogite formed as a suprasubduction, fore-arc ophiolite at ~530 Ma and was isolated far enough from continental crust in order for it to have an entirely juvenile signature. Eclogite facies metamorphism occurred at ~490 Ma, after which we argue for prompt exhumation to higher crustal levels rather than residence in the deep crust for hundreds of millions of years. It is unlikely that the Attunga eclogite is associated with either the Delamerian or Lachlan orogens or that these older orogens underlie the New England Orogen given the complete lack of any Lachlan-derived blocks (e.g., quartzites) within the serpentinite mélange. The Attunga eclogite represents remnants of the offscraped (underplated) and

subducted portions of a structurally overlying Cambrian fore-arc ophiolite (Weraerai terrane). It is now recognized that around three quarters of subduction systems are tectonically erosive and only one quarter accretionary [*Von Huene and Scholl*, 1991]. Therefore, we suggest that the Attunga eclogite represents the tectonically eroded and subducted equivalent of gabbroic material of the Cambrian ophiolitic Weraerai terrane that would have been positioned on the overriding plate in a fore-arc intra-oceanic setting.

8. Conclusions

1. The protolith of the Attunga eclogite within the serpentinite mélange of the Weraerai terrane of the New England Orogen has transitional MORB to suprasubduction zone geochemical affinities. It contains relict magmatic (high U, Th/U) zircon cores with a U-Pb age of 534 ± 14 Ma. This is the same as zircon ages obtained from nearby ophiolitic gabbro within serpentinite mélange at Bingara [*Aitchison and Ireland*, 1995], suggesting that they are tectonically eroded and subducted elements of the same suprasubduction zone ophiolite.
2. Low U, Th/U recrystallized zircon of metamorphic origin formed at 490 ± 14 Ma and shows variable depletion of heavy rare earth elements relative to igneous zircon and no Eu anomalies. Therefore, this zircon records eclogite facies metamorphism that occurred some 40 Ma after formation of the ophiolitic protolith of the Weraerai terrane. The mean initial $\varepsilon Hf_{(t)}$ of the zircons is +13.5 ± 0.8. Thus, the protolith represents juvenile Cambrian crust that experienced eclogite facies metamorphism shortly after it formed and therefore did not originate in a continental margin or back-arc setting.
3. Depletion of HREE in garnet rims and element partitioning between type II zircon/garnet strongly indicate that garnet rims formed coeval to the formation of recrystallized zircon at 490 ± 14 Ma. This latter U-Pb zircon age represents eclogite facies metamorphism.
4. The integrated whole-rock geochemistry and zircon isotope data suggest that the Attunga eclogite formed in an oceanic realm far from any continental influence and was later accreted onto the Gondwanan margin during the latest Devonian collision of the island arc Gamilaroi terrane.
5. The Attunga results require that in the early Paleozoic, eastern Gondwana margin grew by combination of two alternating tectonic processes: (1) westerly dipping subduction beneath Gondwana to produce an Andean-type continental margin and (2) collision and accretion of exotic oceanic terranes via east dipping subduction zones. Given that the disrupted mélange of the Weraerai terrane is situated adjacent the Gamilaroi and Djungati terranes, it is possible that it represents the basement oceanic crustal material on which the younger island arc and accretionary complex developed during the Siluro-Devonian, before collision with Gondwana during the latest Devonian.

Acknowledgments
Support to R.J. Manton, S. Buckman, and A.P. Nutman was provided via GeoQuEST Research Centre of the University of Wollongong. R.J. Manton thanks D. Adams from Macquarie University for assistance with the electron microprobe. V. Bennett thanks S. Eggins for ANU-Neptune access and L. Kinsley for assistance with instrument setup. All data for this paper are properly cited and referred to in the reference list.

References

Agard, P., P. Monié, W. Gerber, J. Omrani, M. Molinaro, M. B. Meyer, L. Labrousse, B. Vrielynck, L. Jolivet, and P. Yamato (2006), Transient, synobduction exhumation of Zagros blueschists inferred from P-T, deformation, time, and kinematic constraints: Implications for Neotethyan wedge dynamics, *J. Geophys. Res.*, *111*, B11401, doi:10.1029/2005JB004103.

Agard, P., P. Yamato, L. Jolivet, and E. Burov (2009), Exhumation of oceanic blueschists and eclogites in subduction zones: Timing and mechanisms, *Earth Sci. Rev.*, *92*, 53–79.

Aitchison, J. C., and S. Buckman (2012), Accordion vs. Quantum tectonics: Insights into continental growth processes from the Paleozoic of eastern Gondwana, *Gondwana Res.*, *22*, 674–680.

Aitchison, J. C., and P. G. Flood (1992), Early Permian transformation margin development of the southern New England Orogen, eastern Australia (eastern Gondwana), *Tectonics*, *11*, 1385–1391, doi:10.1029/92TC01003.

Aitchison, J., and P. Flood (1994), Gamilaroi Terrane: A Devonian rifted intra-oceanic island-arc assemblage, NSW, Australia, in *Volcanism Associated With Extension at Consuming Plate Margins*, *Geol. Soc. London, Spec. Publ.*, vol. 81, edited by J. L. Smellie, pp. 155–168.

Aitchison, J. C., and T. R. Ireland (1995), Age profile of ophiolitic rocks across the Late Palaeozoic New England Orogen, New South Wales: Implications for tectonic models, *Aust. J. Earth Sci.*, *42*, 11–23.

Aitchison, J. C., T. R. Ireland, J. M. C. Blake, and P. G. Flood (1992), 530 Ma zircon age for ophiolite from the New England orogen: Oldest rocks known from eastern Australia, *Geology*, *20*, 125–128.

Aitchison, J. C., J. M. C. Blake, P. G. Flood, and A. S. Jayko (1994), Paleozoic ophiolitic assemblages within the southern New England orogen of eastern Australia: Implication for growth of the Gondwana margin, *Tectonics*, *13*, 1135–1149, doi:10.1029/93TC03550.

Aitchison, J. C., J. M. C. Stratford, and S. Buckman (1997), Geology of the Upper Barnard region: Evidence of Early Permian oblique-slip faulting along the Peel-Manning Fault System of section, in *Tectonics and Metallogenesis of the New England Orogen*, *Spec. Publ*, edited by P. M. Ashley and P. G. Flood, pp. 188–196, Geological Society of Australia, Armidale.

Allan, A. D., and E. C. Leitch (1992), The nature and origin of eclogite blocks in serpentinite from the Tamworth Belt, New England Fold Belt, eastern Australia, *Aust. J. Earth Sci.*, *39*, 29–35.

Anczkiewicz, R., J. P. Platt, M. F. Thirlwall, and J. Wakabayashi (2004), Franciscan subduction off to a slow start: Evidence from high-precision Lu–Hf garnet ages on high grade-blocks, *Earth Planet. Sci. Lett.*, *225*, 147–161.

Arculus, R. J., H. Lapierre, and E. Jaillard (1999), Geochemical window into subduction and accretion processes: Raspas metamorphic complex, Ecuador, *Geology*, *27*, 547–550.

Arenas, R., S. Sánchez Martínez, A. Gerdes, R. Albert, R. Díez Fernández, and P. Andonaegui (2014), Re-interpreting the Devonian ophiolites involved in the Variscan suture: U–Pb and Lu–Hf zircon data of the Moeche Ophiolite (Cabo Ortegal Complex, NW Iberia), *Int. J. Earth Sci.*, *103*, 1385–1402.

Ballard, J. R., J. M. Palin, and I. H. Campbell (2002), Relative oxidation states of magmas inferred from Ce(IV)/Ce(III) in zircon: Application to porphyry copper deposits of northern Chile, *Contrib. Mineral. Petrol.*, *144*, 347–364.

Benson, B. A. (1913), The geology and petrology of the Great Sepentine Belt of New South Wales: Part 1, *Linnean Soc. New South Wales Proc.*, *38*, 490–517.

Black, L. P., et al. (1997), *Dating Tasmania's Oldest Geological Events*, Australian Geol. Surv. Organisation, Canberra.

Black, L. P., S. L. Kamo, C. M. Allen, J. N. Aleinikoff, D. W. Davis, R. J. Korsch, and C. Foudoulis (2003), TEMORA: A new zircon standard for Phanerozoic U–Pb geochronology, *Chem. Geol.*, *200*, 155–170.

Blake, M. C., Jr., and B. L. Murchey (1988), A California model for the New England fold belt, *Quart. Notes Geol. Surv. New South Wales*, *72*, 1–9.

Bouvier, A., J. D. Vervoort, and P. J. Patchett (2008), The Lu–Hf and Sm–Nd isotopic composition of CHUR: Constraints from unequilibrated chondrites and implications for the bulk composition of terrestrial planets, *Earth Planet. Sci. Lett.*, *273*, 48–57.

Breyley, R. (1990), Paling Yard-Upper Bingara: Geology of the Weraerai and Djungati terranes, honours thesis, Univ. of New England, Armidale, Australia.

Brown, M. (2009), *Metamorphic Patterns in Orogenic Systems and the Geological Record in Accretionay Orogens in Space and Time*, *Geol. Soc. London, Spec. Publ.*, vol. 318, edited by P. A. Cawood and A. Kröner, pp. 37–74.

Bryant, C. J., R. J. Arculus, and B. W. Chappell (1997), Clarence River Supersuite: 250 Ma cordilleran tonalitic I-type intrusions in eastern Australia, *J. Petrol.*, *38*, 975–1001.

Buckman, S., A. P. Nutman, J. C. Aitchison, J. Parker, S. Bembrick, T. Line, H. Hidaka, and T. Kamiichi (2014a), The Watonga Formation and Tacking Point Gabbro, Port Macquarie, Australia: Insights into crustal growth mechanisms on the eastern margin of Gondwana, *Gondwana Res.*, *28*, 133–151.

Buckman, S., A. P. Nutman, R. J. Manton, and J. J. Richardson (2014b), Mechanisms of continental growth along eastern Gondwana during the Palaeozoic: Alternating periods of terrane accretion and continental magmatic flare-ups, paper presented at Australian Earth Sciences Convention AESC, Newcastle.

Burov, E. B., L. Jolivet, L. Le Pourhiet, and A. Poliakov (2001), A thermomechanical model of exhumation of HP and UHP methamorphic rocks in Alpine mountain belts, *Tectonophysics*, *342*, 113–136.

Camacho, A., W. Compston, M. McCulloch, and I. McDougall (1997), Timing and exhumation of eclogite facies shear zones, Musgrave Block, central Australia, *J. Metamorph. Geol.*, *15*, 735–751.

Caprarelli, G., and E. C. Leitch (1998), Magmatic changes during the stabilisation of a cordilleran fold belt: The Late Carboniferous-Triassic igneous history of eastern New South Wales, Australia, *Lithos*, *45*, 413–430.

Carswell, D. A. (1990), *Eclogite Facies Rocks*, Chapman & Hall, Glasgow, London: Blackie; New York.

Carswell, D. A., and R. Y. Zhang (1999), Petrographic characteristics and metamorphic evolution of ultrahigh-pressure eclogites in plate-collision belts, *Int. Geol. Rev.*, *41*, 781–798.

Cas, R. A. (1983) *A Review of the Palaeogeography of the Lachlan Fold Belt, Southeastern Australia*, *Spec. Publ.*, vol. 10, Geological Society, Australia.

Cawood, P. A. (1982), Structural relations in the subduction complex of the Paleozoic New England Fold Belt, eastern Australia, *J. Geol.*, *90*, 381–392.

Cawood, P. A. (1983), Modal composition and detrital clinopyroxene geochemistry of lithic sandstones from the New England Fold Belt (east Australia): A Paleozoic forearc terrane, *Geol. Soc. Am. Bull.*, *94*, 1199–1214.

Cawood, P. A. (1984), The development of the SW pacific margin of Gondwana: Correlations between the Rangitata and New England orogens, *Tectonics*, *3*, 539–553, doi:10.1029/TC003i005p00539.

Cawood, P. A. (2005), Terra Australis Orogen: Rodinia breakup and development of the Pacific and Iapetus margins of Gondwana during the Neoproterozoic and Paleozoic, *Earth Sci. Rev.*, *69*, 249–279.

Cawood, P. A., and C. Buchan (2007), Linking accretionary orogenesis with supercontinent assembly, *Earth Sci. Rev.*, *82*, 217–256.

Cawood, P. A., A. Kröner, W. J. Collins, T. M. Kusky, W. D. Mooney, and B. F. Windley (2009), Accretionary orogens through Earth history of section, *Geol. Soc. London, Spec. Publ.*, *318*, 1–36.

Cawood, P. A., E. C. Leitch, R. E. Merle, and A. A. Nemchin (2011), Orogenesis without collision: Stabilizing the Terra Australis accretionary orogen, eastern Australia, *Geol. Soc. Am. Bull.*, *123*, 2240–2255.

Cayley, R. A. (2011), Exotic crustal block accretion to the eastern Gondwanaland margin in the Late Cambrian–Tasmania, the Selwyn Block, and implications for the Cambrian–Silurian evolution of the Ross, Delamerian, and Lachlan orogens, *Gondwana Res.*, *19*, 628–649.

Chalot-Prat, F., J. Ganne, and A. Lombard (2003), No significant element transfer from the oceanic plate to the mantle wedge during subduction and exhumation of the Tethys lithosphere (Western Alps), *Lithos*, *69*, 69–103.

Chemenda, A. I., M. Mattauer, J. Malavieille, and A. N. Bokun (1995), A mechanism for syncollision rock exhumation and associated normal faulting: Results from physical modelling, *Earth Planet. Sci. Lett.*, *132*, 225–232.

Cheng, H., C. J. Zhang, D. Vervoort, X. Li, Q. Li, Y. Wu, and S. Zheng (2012), Timing of eclogite facies metamorphism in the North Qinling by U–Pb and Lu–Hf geochronology, *Lithos*, *136-139*, 46–59.

Clarke, G. L., J. C. Aitchison, and D. Cluzel (1997), Eclogite and blueschists of the Pan Peninsula, NE new Caledonia: A reappraisal, *J. Petrol.*, *38*, 843–876.

Cloos, M. (1982), Flow melanges: Numerical modeling and geologic constraints on their origin in the Franciscan subduction complex, California, *Geol. Soc. Am. Bull.*, *93*, 330–345.

Cloos, M. (1993), Lithospheric buoyancy and collisional orogenesis: Subduction of oceanic plateaus, continental margins, island arcs, spreading ridges, and seamounts, *Geol. Soc. Am. Bull.*, *105*, 715–737.

Cluzel, D., J. C. Aitchison, and P. Christian (2001), Tectonic accretion and underplating of mafic terranes in the Late Eocene intraoceanic fore-arc of New Caledonia (Southwest Pacific): Geodynamic implications, *Techonophysics*, *340*, 23–59.

Collins, W. J. (2002), Nature of extensional accretionary orogens, *Tectonics*, *21*(4), 1024, doi:10.1029/2000TC001272.

Collins, W. J., and R. H. Vernon (1992), Palaeozoic arc growth, deformation and migration across the Lachlan Fold Belt, southeastern Australia, *Tectonophysics*, *214*, 381–400.

Compston, W., I. S. Williams, and C. Meyer (1984), U-Pb geochronology of zircons from lunar breccia 73217 using a sensitive high mass-resolution ion microprobe, *J. Geophys. Res.*, *89*, B525–B534.

Coney, P. J. (1990), The regional tectonics of the Tasman orogenic system, eastern Australia, *J. Struct. Geol.*, *12*, 519–543.

Corbett, G. J. (1976), A new fold structure in the Woolomin beds suggesting a sinistral movement on the peel fault, *J. Geol. Soc. Aust.*, *23*, 401–406.

Corfield, R. I., M. P. Searle, and O. R. Green (1999), Photang thrust sheet: An accretionary complex structurally below the Spontang ophiolite constraining timing and tectonic environment of ophiolite obduction, Ladakh Himalaya, NW India, *J. Geol. Soc. London*, *156*, 1031–1044.
Corfu, F., J. M. Hanchar, P. W. O. Hoskin, and P. Kinny (2003), Atlas of zircon textures, *Rev. Mineral. Geochem.*, *53*, 469–500.
Crawford, A. J., S. Meffre, and P. A. Symonds (2003), 120 to 0 Ma tectonic evolution of the southwest Pacific and analogous geological evolution of the 600 to 220 Ma Tasman Fold Belt System, in *Evolution and Dynamics of the Australian Plate*, *Spec. Publ.*, vol. 372, edited by R. R. Hillis and R. D. Mueller, pp. 377–397, Geological Society, Australia.
Cross, K. C. (1983), The Pigna Barney ophiolitic complex and associated basaltic rocks, northeastern New South Wales, Australia, PhD thesis, Univ. of New England, Armidale, Australia.
Cross, K. C., C. L. Fergusson, and P. G. Flood (1987), Contrasting structural styles in the Paleozoic subduction complex of the Southern New England Orogen, Eastern Australia, in *Terrane Accretion and Orogenic Belts*, vol. 19, edited by E. C. Leitch and E. Scheibner, pp. 83–92, AGU Geodynamics, Washington D. C.
Cumming, G. L., and J. R. Richards (1975), Ore lead isotope ratios in a continuously changing Earth, *Earth Planet. Sci. Lett.*, *28*, 155–171.
Dewey, J. F., P. D. Ryan, and T. B. Andersen (1993), Orogenic uplift and collapse, crustal thickness, fabrics and metamorphic phase changes: The role of eclogites, *Geol. Soc. London, Spec. Publ.*, *76*, 325–343.
Di Vinchenzo, G., R. Palmeri, F. Talarico, P. A. M. Andriessen, and C. A. Ricci (1997), Petrology and geochronology of eclogites from the Lanterman Range, Antarctica, *J. Petrol.*, *38*, 1392–1417.
Di Vincenzo, G., F. Horton, and R. Palmeri (2016), Protracted (~30 Ma) eclogite-facies metamorphism in northern Victoria Land (Antarctica): Implications for the geodynamics of the Ross/Delamerian Orogen, *Gondwana Res.*, *40*, 91–106.
Ernst, W. G. (1970), Tectonic contact between the Franciscan Mélange and Great Valley Sequence—Crustal expression of a Late Mesozoic Benioff Zone, *J. Geophys. Res.*, *75*, 886–901, doi:10.1029/JB075i005p00886.
Ernst, W. G. (1972), Occurrence and mineralogical evolution of blueschist belts with time, *Am. J. Sci.*, *272*, 657–668.
Ernst, W. G. (1988), Tectonic history of subduction zones inferred from retrograde blueschist P-T paths, *Geology*, *16*, 1081–1084.
Ernst, W. G. (2001), Subduction, ultrahigh-pressure metamorphism, and regurgitation of buoyant crustal slices—Implications for arcs and continental growth, *Phys. Earth Planet. Inter.*, *127*, 253–275.
Ferry, J. M., and E. B. Watson (2007), New thermodynamic models and revised calibrations for the Ti-in-zircon and Zr-in-rutile thermometers, *Contrib. Mineral. Petrol.*, *154*, 429–437.
Fergusson, C. L. (2003), Ordovician-Silurian accretion tectonics of the Lachlan Fold Belt, southeastern Australia, *Aust. J. Earth Sci.*, *50*, 475–490.
Fergusson, C. L., and P. J. Coney (1992), Convergence and intraplate deformation in the Lachlan Fold Belt of southeastern Australia, *Techonophysics*, *214*, 417–439.
Fergusson, C. L., A. P. Nutman, T. Kamiichi, and H. Hidaka (2013), Evolution of a Cambrian active continental margin: The Delamerian–Lachlan connection in southeastern Australia from a zircon perspective, *Gondwana Res.*, *24*, 1051–1066.
Fitzherbert, J. A., G. L. Clarke, B. Marmo, and R. Powell (2004), The origin and *P-T* evolution of peridotites and serpentinites of NE New Caledonia: Prograde interaction between continental margin and the mantle wedge, *J. Metamorph. Geol.*, *22*, 327–344.
Flood, P. G., and J. C. Aitchison (1988), Tectonostratigraphic terranes of the southern part of the New England Orogen of section, in *New England Orogen Tectonics and Metallogenesis*, *Department of Geology and Geophysics*, edited by J. D. Keleeman, pp. 7–10, Univ. of New England.
Foden, J., M. Elburg, J. Dougherty-Page, and A. Burtt (2006), The timing and duration of the Delamerian Orogeny: Correlation with the Ross Orogen and implications for Gondwana assembly, *J. Geol.*, *114*, 291–210.
Foster, D. A., and D. R. Gray (2000), Evolution and structure of the Lachlan Fold Belt (Orogen) of eastern Australia, *Annu. Rev. Earth Planet. Sci.*, *28*, 47–80.
Fryer, P., C. G. Wheat, and M. J. Mottl (1999), Mariana blueschist mud volcanism: Implications for conditions within the subduction zone, *Geology*, *27*, 103–106.
Fukui, S., T. Watanabe, T. Itaya, and E. Leitch (1995), Middle Ordovician high PT metamorphic rocks in eastern Australia: Evidence from K-Ar age, *Tectonics*, *14*, 1014–1020, doi:10.1029/94TC01317.
Fukui, S., T. Tsujimori, T. Watanabe, and T. Itaya (2012), Tectono-metamorphic evolution of high-P/T and low-P/T metamorphic rocks in the Tia Complex, southern New England Fold Belt, eastern Australia: Insights from K-Ar chronology, *J. Asian Earth Sci.*, *59*, 62–69.
Furey-Greig, T. (1999), Late Ordovician conodonts from the olistostromal Wisemans Arm Formation (New England Region, Australia), *Abhandlungen der Geologischen Bundesanstalt*, *54*, 303–314.
Furey-Greig, T. (2000), Late Ordovician (Eastonian) conodonts from the Early Devonian Drik Drik Formation, Woolomin area, eastern Australia, *Records Western Aust. Museum Suppl.*, *58*, 133–143.
Goffé, B., and C. Chopin (1986), High-pressure metamorphism in the Western Alps: Zoneography of metapelites, chronology and consequences, *Schweiz. Mineral. Petrogr. Mitt.*, *66*, 41–52.
Gerdes, A., and A. Zeh (2009), Zircon formation versus zircon alteration—New insights from combined U–Pb and Lu–Hf in-situ LA-ICP-MS analyses, and consequences for the interpretation of Archean zircon from the central zone of the Limpopo Belt, *Chem. Geol.*, *261*, 230–243.
Gebauer, D., H. P. Schertl, M. Brix, and W. Schreyer (1997), 35 Ma old ultrahigh-pressure metamorphism and evidence for very rapid exhumation in the Dora Maira Massif, Western Alps, *Lithos*, *41*, 5–24.
Gilotti, J. A., A. P. Nutman, and H. K. Brueckner (2004), Devonian to Carboniferous collision in the Greenland Caledonides: U-Pb zircon and Sm-Nd ages of high-pressure and ultrahigh-pressure metamorphism, *Contrib. Mineral. Petrol.*, *148*, 216–235.
Glen, R. A. (2005), The Tasmanides of eastern Australia of section, *Geol. Soc. London, Spec. Publ.*, *246*, 23–96.
Glen, R. A. (2013), Refining accretionary orogen models for the Tasmanides of eastern Australia, *Aust. J. Earth Sci.*, *60*, 315–370.
Glen, R. A., and S. Meffre (2009), Styles of Cenozoic collisions in the western and southwestern Pacific and their applications to Palaeozoic collisions in the Tasmanides of eastern Australia, *Tectonophysics*, *479*, 130–149.
Glen, R. A., J. L. Walshe, L. M. Barron, and J. J. Watkins (1998), Ordovician convergent-margin volcanism and tectonism in the Lachlan sector of east Gondwana, *Geology*, *26*, 751–754.
Glen, R. A., S. Meffre, and R. J. Scott (2007), Benambran orogeny in the eastern Lachlan Orogen, Australia, *Aust. J. Earth Sci.*, *54*, 385–415.
Glen, R. A., I. G. Percival, and C. D. Quinn (2009), Ordovician continental margin terranes in the Lachlan Orogen, Australia: Implications for tectonics in an accretionary orogen along the east Gondwana margin, *Tectonics*, *28*, TC6012, doi:10.1029/2009TC002446.
Glen, R. A., A. Saeed, C. D. Quinn, and W. L. Griffin (2011), U–Pb and Hf isotope data from zircons in the Macquarie Arc, Lachlan Orogen: Implications for arc evolution and Ordovician palaeogeography along part of the east Gondwana margin, *Gondwana Res.*, *19*, 670–685.
Gray, D. R., and D. A. Foster (2004), Tectonic evolution of the Lachlan Orogen, southeast Australia: Historical review, data synthesis and modern perspectives, *Aust. J. Earth Sci.*, *51*, 773–817.

Griffin, W. L., E. A. Belousova, S. R. Shee, N. J. Pearson, and S. Y. O'reilly (2004), Archean crustal evolution in the northern Yilgarn Craton: U–Pb and Hf-isotope evidence from detrital zircons, *Precambrian Res.*, *131*, 231–282.
Guillot, S., K. H. Hattori, J. de Sigoyer, T. Nägler, and A.-L. Auzende (2001), Evidence of hydration of the mantle wedge and its role in the exhumation of eclogites, *Earth Planet. Sci. Lett.*, *193*, 115–127.
Guillot, S., S. Schwartz, K. Hattori, A. Auzende, and J. Lardeaux (2004), The Monviso ophiolitic massif (Western Alps), a section through a serpentinite subduction channel, *J. Virtual Explorer*, *16*, 17.
Guillot, S., K. Hattori, P. Agard, S. Schwartz, and O. Vidal (2009), Exhumation processes in oceanic and continental subduction contexts: A review, in *Subduction Zone Geodynamics*, edited by S. Lallemand and F. Funiciello, pp. 175–205, Springer, Berlin Heidelberg.
Hadlari, T., W. J. Davis, and K. Dewing (2013), A pericratonic model for the Pearya terrane as an extension of the Franklinian margin of Laurentia, Canadian Arctic, *Geol. Soc. Am. Bull.*, *126*, 182–200.
Hacker, B. R., G. A. Abers, and S. M. Peacock (2003), Subduction factory: Theoretical mineralogy, density, seismic wave speeds, and H_2O content, *J. Geophys. Res.*, *108*(B1), 2029, doi:10.1029/2001JB001127.
Hacker, B. R., S. R. Wallis, L. Ratschbacher, M. Grove, and G. Gehrels (2006), High-temperature geochronology constraints on the tectonic history and architecture of the ultrahigh-pressure Dabie-Sulu Orogen, *Tectonics*, *25*, TC5006, doi:10.1029/2005TC001937.
Hacker, B. R., L. Ratschbacher, L. Webb, T. R. Ireland, D. Walker, and D. Shuwen (1998), U/Pb zircon ages constrain the architecture of the ultrahigh-pressure Qinling-Dabie Orogen, China, *Earth Planet. Sci. Lett.*, *161*, 215–230.
Haines, P. W., S. P. Turner, J. D. Foden, and J. B. Jago (2009), Isotopic and geochemical characterisation of the Cambrian Kanmantoo Group, South Australia: Implications for stratigraphy and provenance, *Aust. J. Earth Sci.*, *56*, 1095–1110.
Harlow, G. E., S. R. Hemming, H. G. Avé Lallemant, V. B. Sisson, and S. S. Sorensen (2004), Two high-pressure–low-temperature serpentinite-matrix mélange belts, Motagua fault zone, Guatemala: A record of Aptian and Maastrichtian collisions, *Geology*, *32*, 17–20.
Hawthorne, F. C., R. Oberti, G. E. Harlow, W. V. Maresch, R. F. Martin, J. C. Schumacher, and M. D. Welch (2012), Nomenclature of the amphibole supergroup, *Am. Mineral.*, *97*, 2031–2048.
Hermann, J., D. Rubatto, A. Korsakov, and V. S. Shartsky (2001), Multiple zircon growth during fast exhumation of diamondiferous, deeply subducted continental crust (Kokchetav Massif, Kazakhstan), *Contrib. Mineral. Petrol.*, *141*, 66–82.
Hiess, J., V. C. Bennett, A. P. Nutman, and I. S. Williams (2009), In situ U–Pb, O and Hf isotopic compositions of zircon and olivine from Eoarchaean rocks, West Greenland: New insights to making old crust, *Geochim. Cosmochim. Acta*, *73*, 4489–4516.
Holland, T. J. B. (1983), The experimental determination of activities in disordered and short-range ordered jadeitic pyroxenes, *Contrib. Mineral. Petrol.*, *82*, 214–220.
Hoskin, P. W. O., and L. P. Black (2000), Metamorphic zircon formation by solid-state recrystallization of protolith igneous zircon, *J. Metamorph. Geol.*, *18*, 423–439.
Hourigan, J. K., M. T. Brandon, A. V. Soloviev, A. B. Kirmasov, J. I. Garver, J. Stevenson, and P. W. Reiners (2009), Eocene arc-continent collision and crustal consolidation in Kamchatka, Russian Far East, *Am. J. Sci.*, *309*, 333–396.
Huang, C. Y., C. W. Chien, B. Yao, and C. P. Chang (2008), The Lichi Mélange: A collision mélange formation along early arcward backthrusts during forearc basin closure, Taiwan arc-continent collision of section, in *Formation and Applications of the Sedimentary Record in Arc Collision Zone*, *Special Paper*, vol. 436, edited by A. E. Draut et al., pp. 127–154, Geological Society, America.
Jackson, S. E., N. J. Pearson, W. L. Griffin, and E. A. Belousova (2004), The application of laser ablation microprobe-inductively coupled plasma-mass spectrometry (LAM-ICPMS) to in situ U–Pb zircon geochronology, *Chem. Geol.*, *211*, 47–69.
Jayko, A. S., M. C. Blake Jr., and J. C. Aitchison (1993), Structural uplift of ophiolitic slivers along major faults of the New Engand Orogen, in *New England Orogen, Eastern Australia*, edited by P. G. Flood and J. C. Aitchison, pp 163–180, Univ. of New England, Armidale, N. S. W.
Jolivet, L., C. Faccenna, B. Goffé, E. Burov, and P. Agard (2003), Subduction tectonics and exhumation of high-pressure metamorphic rocks in the Mediterranean orogens, *Am. J. Sci.*, *303*, 353–409.
Kelley, S. (2002), Excess argon in K–Ar and Ar–Ar geochronology, *Chem. Geol.*, *188*, 1–22.
Kemp, A. I. S., C. J. Hawkesworth, W. J. Collins, C. M. Gray, and P. L. Blevin (2009), Isotopic evidence for rapid continental growth in an extensional accretionary orogen: The Tasmanides, eastern Australia, *Earth Planet. Sci. Lett.*, *284*, 455–466.
Korsch, R. J., and H. J. Harrington (1987), Oroclinal bending, fragmentation and deformation of terranes in the New England Orogen, eastern Australia of section, in *Terrane Accretion and Orogenic Belts*, edited by E. C. Leitch and E. Scheibner, pp. 129–139, AGU, Washington, D. C.
Korsch, R. J., D. W. Johnston, and K. D. Wake-dyster (1997), Crustal architecture of the New England Orogen based on deep seismic reflection profiling, in *Tectonics and Metallogenesis of the New England Orogen*, *Spec. Publ.*, vol. 19, edited by P. M. Ashley and P. G. Flood, pp. 29–51, Geological Society, Australia.
Krogh Rav2na, E. J., and J. Paquin (2003), Thermobarometric methodologies applicable to eclogites and garnet ultrabasites, *EMU Notes Mineral.*, *5*, 229–259.
Krogh Ravna, E. J., and M. P. Terry (2004), Geothermobarometry of UHP and HP eclogites and schists—An evaluation of equilibria among garnet-clinopyroxene-kyanite-phengite-coesite/quartz, *J. Metamorph. Geol.*, *22*, 579–592.
Lanphere, M. A., and J. J. Hockley (1976), The age of nephrite occurrences in the great serpentine belt of New South Wales, *J. Geol. Soc. Aust.*, *23*, 15–17.
Leitch, E. C. (1975), Plate tectonic interpretation of the Paleozoic history of the New England fold belt, *Geol. Soc. Am. Bull.*, *86*, 141.
Leitch, E. C. (1980), The great serpentinite belt of New South Wales: Diverse mafic-ultramafic complexes set in a Paleozoic arc, paper presented at Proceedings of the International Ophiolite Symposium, Cyprus.
Liati, A., and D. Gebauer (1999), Constraining the prograde and retrograde P-T-t path of Eocene HP rocks by SHRIMP dating of different zircon domains: Inferred rates of heating, burial, cooling and exhumation for central Rhodope, northern, *Greece Contrib. Mineral. Petrol.*, *135*, 340–354.
Ludwig, K. R. (2003), *Isoplot 3.0: A Geochronological Toolkit for Microsoft Excel*, *Berkeley Geochronological Center Special Publication*, vol. 4, Berkeley Geochronological Center, Berkeley, Calif.
McPhie, J. (1987), Andean analogue for Late Carboniferous volcanic arc and arc flank environments of the western New England Orogen, New South Wales, Australia, *Tectonicophysics*, *13*, 269–288.
Martínez, J. C., J. A. Dristas, and H.-J. Massonne (2012), Palaeozoic accretion of the microcontinent Chilenia, North Patagonian Andes: High-pressure metamorphism and subsequent thermal relaxation, *Int. Geol. Rev.*, *54*, 472–490.
Maruyama, S., J. G. Liou, and M. Terabayashi (1996), Blueschists and eclogites of the world and their exhumation, *Int. Geol. Rev.*, *38*, 485–594.
Medaris, L. G. (1999), Garnet peridotites in Eurasian high-pressure and ultrahigh-pressure terranes: A diversity of origins and thermal histories, *Int. Geol. Rev.*, *41*, 799–815.
Morimoto, N., J. Fabries, A. K. Ferguson, I. V. Ginzburg, M. Ross, F. A. Seifert, J. Zussman, K. Aoki, and G. Gottardi (1988), Nomenclature of pyroxenes, *Am. Mineral.*, *73*, 1123–1133.

Nekrasov, G. E., and E. S. Bogomolov (2015), Ophiolites of the Ust-Belskii terrane (Chukotka): A consequence of late Precambrian breakup of the Rodinia supercontinent in structures of the NE framing of the Siberian craton (structural, petrological-mineralogical, and isotope data), *Dokl. Earth Sci.*, *461*, 351–355.
Norman, M. D., N. J. Pearson, A. Sharma, and W. L. Griffin (1996), Quantitative analysis of trace elements in geological materials by laser ablation ICPMS: Instrumental operating conditions and calibration values of NIST glasses, *Geostand. Newslett.*, *20*, 247–261.
Nowell, G. M., P. D. Kempton, S. R. Noble, J. G. Fitton, A. D. Saunders, J. J. Mahoney, and R. N. Taylor (1998), High precision Hf isotope measurements of MORB and OIB by thermal ionisation mass spectrometry: Insights into the depleted mantle, *Chem. Geol.*, *149*, 211–233.
Nutman, A. P., F. Kalsbeek, and C. R. L. Friend (2008), The Nagssugtoqidian orogen in South-East Greenland: Evidence for Paleoproterozoic collision and plate assembly, *Am. J. Sci.*, *308*, 529–572.
Nutman, A. P., S. Buckman, H. Hidaka, T. Kamiichi, E. Belousova, and J. Aitchison (2013), Middle Carboniferous-Early Triassic eclogite–blueschist blocks within a serpentinite mélange at Port Macquarie, eastern Australia: Implications for the evolution of Gondwana's eastern margin, *Gondwana Res.*, *24*, 1038–1050.
Och, D. J., E. C. Leitch, G. Capparelli, and T. Watanabe (2003), Blueschist and eclogite in tectonic melange, Port Maquarie, New South Wales, Australia, *Mineral. Mag.*, *67*, 609–624.
Och, D. J., E. C. Leitch, and G. Caprarelli (2007), Geological units of the Port Macquarie-Tacking Point tract, north-eastern Port Macquarie Block, Mid North Coast region of New South Wales, *Quart. Notes Geol. Surv. New South Wales*, *126*, 20.
Offler, R. (1999), Origin and significance of blueschist "knockers", Glenrock Station, NSW, in *New England Orogen: Regional Geology, Tectonics and Metallogenesis*, edited by P. G. Flood, pp. 35–44, Department of Geology and Geophysics, Univ. of New England, Armidale, N. S. W.
Offler, R., and A. J. Williams (1987), Evidence for sinistral movement on the Peel Fault System in serpentinites, Glenrock Station, NSW, *Geodynamics*, *19*, 141–151.
Offler, R., and S. Shaw (2006), Hornblend gabbro block in serpentininte melange, Peel-Manning Fault System NSW Australia, *J. Geol.*, *114*, 211–230.
Offler, R., and D. A. Foster (2008), Timing and development of oroclines in the southern New England Orogen, New South Wales, *Aust. J. Earth Sci.*, *55*, 331–340.
Offler, R., and C. Murray (2011), Devonian volcanics in the New England Orogen: Tectonic setting and polarity, *Gondwana Res.*, *19*, 706–715.
Offler, R., D. S. O'Hanley and P. G. Lennox (1989), Kinematic indicators in serpentinites—The Peel-Manning Fault System: A test case, Australasian Tectonics Conference (SGTSG) Kingscote, Kangaro Island S.A. Abstract 110-111.
Ota, T., and Y. Kaneko (2010), Blueschists, eclogites, and subduction zone tectonics: Insights from a review of Late Miocene blueschists and eclogites, and related young high-pressure metamorphic rocks, *Gondwana Res.*, *18*, 167–188.
Patchett, P. J., O. Kouvo, C. E. Hedge, and M. Tatsumoto (1981), Evolution of continental crust and mantle heterogeneity: Evidence from Hf isotopes, *Contrib. Mineral. Petrol.*, *79*, 279–297.
Pearce, J., and J. R. Cann (1973), Tectonic setting of basic volcanic rocks determined using trace element analysis, *Earth Planet. Sci. Lett.*, *19*, 290–300.
Pearce, J. A. (2008), Geochemical fingerprinting of oceanic basalts with applications to ophiolite classification and the search for Archean oceanic crust, *Lithos*, *100*, 14–48.
Phillips, G., and R. Offler (2011), Contrasting modes of eclogite and blueschist exhumation in a retreating subduction system: The Tasmanides, Australia, *Gondwana Res.*, *19*, 800–811.
Phillips, G., R. Offler, D. Rubatto, and D. Phillips (2015), High-pressure metamorphism in the southern New England Orogen: Implications for long-lived accretionary orogenesis in eastern Australia, *Tectonics*, *34*, 1979–2010, doi:10.1002/2015TC003920.
Platt, J. P. (1986), Dynamics of orogenic wedges and the uplift of high-pressure metamorphic rocks, *Geol. Soc. Am. Bull.*, *97*, 1037–1053.
Poli, S. (1993), The amphibolite-eclogite transformation; an experimental study on basalt, *Am. J. Sci.*, *293*, 1061–1107.
Powell, C. M. (1984), Ordovician to earliest Silurian: Marginal sea and island arc—Silurian to mid-Devonian dextral transtensional margin, late Devonian and early carboniferous. Continental magmatic arc along the eastern edge of the Lachlan Fold Belt, in *Phanerozoic Earth History of Australia*, edited by J. J. Veevers, pp. 290–340, Oxford Univ. Press, Oxford.
Ring, U., M. T. Brandon, S. D. Willett, and G. S. Lister (1999), Exhumation processes, *Geol. Soc. London, Spec. Publ.*, *154*, 1–27.
Roberts, J., and B. A. Engel (1987), Depositional and tectonic history of the southern New England Orogen, *Aust. J. Earth Sci.*, *34*, 1–20.
Robertson, A. (2004), Development of concepts concerning the genesis and emplacement of Tethyan ophiolites in the Eastern Mediterranean and Oman regions, *Earth Sci. Rev.*, *66*, 331–387.
Robertson, K., D. Taylor, S. Thiel, and G. Heinson (2015), Magnetotelluric evidence for serpentinisation in a Cambrian subduction zone beneath the Delamerian Orogen, southeast Australia, *Gondwana Res.*, *28*, 601–611.
Rogers, G. (1986), Geology of the northern part of the Great Serpentinite Belt-Bingara to Upper Bingara, honours thesis, Univ. of New England, Australia.
Rubatto, D. (2002), Zircon trace element geochemistry: Partitioning with garnet and the link between U–Pb ages and metamorphism, *Chem. Geol.*, *184*, 123–138.
Rubatto, D., and J. Hermann (2003), Zircon formation during fluid circulation in eclogites (Monviso, Western Alps): Implications for Zr and Hf budget in subduction zones, *Geochim. Cosmochim. Acta*, *67*, 2173–2187.
Rubatto, D., D. Gebauer, and R. Compagnoni (1999), Dating of eclogite-facies zircons: The age of Alpine metamorphism in the Sesia–Lanzo Zone (Western Alps), *Earth Planet. Sci. Lett.*, *167*, 141–158.
Sano, S., R. Offler, H. Hyodo, and T. Watanabe (2004), Geochemistry and chronology of tectonic blocks in serpentinite mélange of the southern New England Fold Belt, NSW, Australia, *Gondwana Res.*, *7*, 817–831.
Scambelluri, M., M. Scambelluri, P. Bottazzi, V. Trommsdorff, R. Vannucci, J. Hermann, J. M. T. Gomez-Pugnaire, and V. L. S. Vizcaino (2001), Incompatible element-rich fuids released by antigorite breakdown in deeply subducted mantle, *Earth Planet. Sci. Lett.*, *192*, 457–470.
Schaltegger, U., C. M. Fanning, D. Gunther, J. C. Maurin, K. Schulmann, and D. Gebauer (1999), Growth, annealing and recrystallization of zircon and preservation of monazite in high-grade metamorphism: Conventional and in-situ U-Pb isotope, cathodoluminescence and microchemical evidence, *Contrib. Mineral. Petrol.*, *134*, 186–201.
Scheibner, E., and R. A. Glen (1972), The Peel Thrust and its tectonic history, *Geol. Surv. New South Wales Quart. Notes*, *8*, 1–14.
Scheibner, E., and H. Basden (1996), *Structural Framework, Geology of New South Wales—Synthesis*, vol. 1, Geological Survey of New South Wales.
Scherer, E., C. Münker, and K. Mezger (2001), Calibration of the lutetium-hafnium clock, *Science*, *293*, 683–687.
Searle, M. P. C., J. Warren, D. J. Waters, and R. R. Parrish (2004), Structural evolution, metamorphism and restoration of the Arabian continental margin, Saih Hatat region, Oman Mountains, *J. Struct. Geol.*, *26*, 451–473.
Shaanan, U., G. Rosenbaum, S. Pisarevsky, and F. Speranza (2015), Paleomagnetic data from the New England Orogen (eastern Australia) and implications for oroclinal bending, *Tectonophysics*, *664*, 182–190.

Shaw, S. E., and R. H. Flood (1974), Eclogite from serpentinite near Attunga, New South Wales, *J. Geol. Soc. Aust.*, *21*, 377–385.
Shaw, S. E., and R. H. Flood (1981), The New England Batholith, eastern Australia: Geochemical variations in time and space, *J. Geophys. Res.*, *86*, 10,530–10,544, doi:10.1029/JB086iB11p10530.
Shaw, S. E., and R. H. Flood (1992), A compilation of Late Permian and Triassic biotite Rb-Sr data from the New England Batholith and areas to the southeast, in *Centre for Isotope Studies Research Report 1991–1992*, edited by P. F. Carr, pp. 151–155, CSIRO Mineral Research Laboratories, North Ryde, N. S. W.
Shervais, J. W. (1982), Ti-V plots and the petrogenesis of modern and ophiolitic lavas, *Earth Planet. Sci. Lett.*, *59*, 101–118.
Söderlund, U., P. J. Patchett, J. D. Vervoort, and C. E. Isachsen (2004), The 176Lu decay constant determined by Lu–Hf and U–Pb isotope systematics of Precambrian mafic intrusions, *Earth Planet. Sci. Lett.*, *219*, 311–324.
Spaggiari, C. V., D. R. Gray, and D. A. Foster (2004), Lachlan Orogen subduction–accretion systematics revisited, *Aust. J. Earth Sci.*, *51*, 549–553.
Spandler, C., and J. Hermann (2006), High-pressure veins in eclogite from New Caledonia and their significance for fluid migration in subduction zones, *Lithos*, *89*, 135–153.
Spandler, C., J. Hermann, R. Arculus, and J. Mavrogenes (2003), Redistribution of trace elements during prograde metamorphism from lawsonite blueschist to eclogite facies: Implications for deep subduction-zone processes, *Contrib. Mineral. Petrol.*, *146*, 205–222.
Spear, F. S. (1993), *Metamorphic Phase Equilibria and Pressure-Temperature-Time Paths*, Mineralogical Society of America, Washington, D. C.
Stern, R. A. (1998), High-resolution SIMS determination of radiogenic tracer-isotope ratios in minerals, in *Modern Approaches to Ore and Environmental Mineralogy. Short Course Series*, edited by L. J. Cabri, and D. J. Vaughan, vol. 27, pp. 241–268, Mineral. Assoc. of Canada, Ottawa, Ontario.
Stewart, I. (1995), Cambrian age for the Pipeclay Creek Formation, Tamworth Belt, northern New South Wales, *Courier Forschungsinstitut*, *182*, 565–566.
Stratford, J. M. C., and J. C. Aitchison (1997), Geochemical evolution within a Devonian intra-oceanic island arc: The Gamilaroi terrane, southern New England orogen, Australia, *Island Arc*, *6*, 213–227.
Sun, S. S., and W. F. McDonough (1989), Chemical and isotopic systematics of oceanic basalts: Implications for mantle composition and processes, *Geol. Soc. London, Spec. Publ.*, *42*, 313–345.
Tian, Z. L., and C. J. Wei (2014), Coexistence of garnet blueschist and eclogite in South Tianshan, NW China: Dependence of *P-T* evolution and bulk-rock composition, *J. Metamorph. Geol.*, *32*, 743–764.
Tomaschek, F., A. K. Kennedy, I. M. Villa, M. Lagos, and C. Ballhaus (2003), Zircons from Syros, Cyclades, Greece—Recrystallization and mobilization of zircon during high-pressure metamorphism, *J. Petrol.*, *44*, 1977–2002.
Vervoort, J. D., P. J. Patchett, U. Söderlund, and M. Baker (2004), Isotopic composition of Yb and the determination of Lu concentrations and Lu/Hf ratios by isotope dilution using MC-ICPMS, *Geochem. Geophys. Geosyst.*, *5*, Q11002, doi:10.1029/2004GC000721.
Vickery, N. M., R. E. Brown, and I. G. Percival (2010), *Manilla 1:100 000 Geological Sheet 9036, Explanatory Notes*, Geological Survey of New South Wales, Maitland.
Von Blanckenburg, F., and J. Huw Davies (1995), Slab breakoff: A model for syncollisional magmatism and tectonics in the Alps, *Tectonics*, *14*, 120–131, doi:10.1029/94TC02051.
Von Huene, R., and D. W. Scholl (1991), Observations at convergent margins concerning sediment subduction, sediment erosion, and the growth of continental crust, *Rev. Geophys.*, *29*, 279–316, doi:10.1029/91RG00969.
Watanabe, T., C. M. Fanning, E. Leitch, and T. Morita (1999), Neoproterozoic Attunga Eclogite in eastern Australia margin, *Gondwana Res.*, *2*, 616.
Watson, E. B., and T. M. Harrison (2005), Zircon thermometer reveals minimum melting conditions on earliest Earth, *Science*, *308*, 841–844.
Watson, E. B., D. A. Wark, and J. B. Thomas (2006), Crystallization thermometers for zircon and rutile, *Contrib. Mineral. Petrol.*, *151*, 413–433.
Wayne, D. M., and A. K. Sinha (1992), Stability of zircon U-Pb systematics in a greenschist-grade mylonite: An example from the Rockfish Valley fault zone, central Virginia, USA, *J. Geol.*, *100*, 593–603.
Wedepohl, H. K. (1995), The composition of the continental crust, *Geochim. Cosmochim. Acta*, *59*, 1217–1232.
Weill, D. F. (1973), Europium anomaly in plagioclase feldspar: Experimental results and semiquantitative model, *Science*, *180*, 1059–1060.
Whitney, D. L., and P. B. Davis (2006), Why is lawsonite eclogite so rare? Metamorphism and preservation of lawsonite eclogite, Sivrihisar, Turkey, *Geology*, *34*, 473–476.
Wilkinson, J. F. G. (1969), The New England Batholith—Ultramafic and associated rocks of northeastern New South Wales, in *The Geology of New South Wales*, vol. 16, edited by G. H. Packham, pp. 299–307, Geological Society, Australia.
Williams, A. (1979), Foliation developments in serpentinites, Glenrock, New South Wales, *Tectonophysics*, *58*, 81–95.
Williams, I. S., I. S. Buick, and I. Cartwright (1996), An extended episode of early Mesoproterozoic metamorphic fluid flow in the Reynolds Range, central Australia, *J. Metamorph. Geol.*, *14*, 29–47.
Williams, I. S. (1998), U–Th–Pb geochronology by ion microprobe, in *Applications of microanalytical techniques to understanding mineralizing processes*, vol. 7, pp. 1–35, Reviews in Economic Geology, Shaffer Parkway, Littleton, Colo.
Willner, A. P., A. Gerdes, H.-J. Massonne, A. Schmidt, M. Sudo, S. N. Thomson, and G. Vujovich (2010), The geodynamics of collision of a microplate (Chilenia) in Devonian times deduced by the pressure–temperature–time evolution within part of a collisional belt (Guarguaraz Complex, W-Argentina), *Contrib. Mineral. Petrol.*, *162*, 303–327.
Woodhead, J., and J. Hergt (2005), A preliminary appraisal of seven natural zircon reference materials for in situ Hf isotope determination, *Geostand. Geoanal. Res.*, *29*, 183–195.
Woodhead, J., J. Hergt, M. Shelley, S. Eggins, and R. Kemp (2004), Zircon Hf-isotope analysis with an excimer laser, depth profiling, ablation of complex geometries, and concomitant age estimation, *Chem. Geol.*, *209*, 121–135.
Yang, K., and P. K. Seccombe (1997), Geochemistry of the mafic and ultramafic complexes of the northern Great Serpentinite Belt, New South Wales: Implications for first stage melting, in *Tectonics and Metallogenesis of the New England Orogen*, *Spec. Publ.*, vol. 19, edited by P. M. Ashley and P. G. Flood, pp. 197–211, Geological Society, Australia.
Zheng, Y., Y. Wu, Z. Zhao, S. Zhang, P. Xu, and F. Wu (2005), Metamorphic effect on zircon Lu–Hf and U–Pb isotope systems in ultrahigh-pressure eclogite-facies metagranite and metabasite, *Earth Planet. Sci. Lett.*, *240*, 378–400.
Zhai, Q.-G., B.-M. Jahn, J. Wang, L. Su, X.-X. Mo, K.-L. Wang, S.-H. Tang, and H.-Y. Lee (2013), The Carboniferous ophiolite in the middle of the Qiangtang terrane, Northern Tibet: SHRIMP U–Pb dating, geochemical and Sr–Nd–Hf isotopic characteristics, *Lithos*, *168–169*, 186–199.
Zhengxin, Y., et al. (2015), Zircon U-Pb geochronology and Hf isotopic constraints on petrogenesis of plagiogranite from Cuomuqu ophiolite Bangong Lake Area, North Tibet, *Acta Geol. Sin.*, *89*, 418–440.
Zucchetto, R. G., R. A. Henderson, B. K. Davis, and R. Wysoczanski (1999), Age constraints on deformation of the eastern Hodgkinson Province, north Queensland: New perspectives on the evolution of the northern Tasman Orogenic Zone, *Aust. J. Earth Sci.*, *46*, 105–114.